**Title:** Megathrust locking encoded in subduction landscapes

**Authors:** *Oryan, B.[1], Olive, J.-A.[1], Jolivet, R[1,2]., Malatesta, L. C.[3], Gailleton, B[4]., and Bruhat, L.[5]*

**Affiliations:**

(1) Laboratoire de Géologie, CNRS - École normale supérieure - PSL University, Paris, France.
(2) Institut Universitaire de France, 1 rue Descartes, 75006 Paris.

(3) Earth Surface Process Modelling, GFZ German Research Center for Geosciences, Potsdam, Germany.

(4) Univ. Rennes, Géosciences Rennes, UMR 6118, 35000 Rennes, France.

(5) Group Risk Management, AXA, Paris, France.

Corresponding author: bar.oryan@columbia.edu

**One Sentence Summary:** Interseismic locking on megathrusts permanently strains the overriding plate, leaving a distinct landscape footprint.

*This paper is a non-peer reviewed preprint submitted to EarthArXiv. It is currently under review at Science Advances*

## Abstract

Locked areas of subduction megathrusts are increasingly found to coincide with landscape features sculpted over hundreds of kyrs, yet the mechanisms that underlie such correlations remain elusive. We show that interseismic locking gradients induce increments of irreversible strain across the overriding plate manifested predominantly as distributed seismicity. Summing these increments over hundreds of earthquake cycles produces a spatially-variable field of uplift representing the unbalance of co-, post-, and interseismic strain. This long-term uplift explains first-order geomorphological features of subduction zones such as: the position of the continental shelf break, the distribution of marine terraces and peninsulas, and the profile of forearc rivers. Inelastic yielding of the forearc thus encodes short-term locking patterns in subduction landscapes, highlighting the role geomorphology can play in constraining Earth's greatest source of seismic hazard.

## Main text

The largest earthquakes on Earth occur at subduction zones, where a dense tectonic plate sinks into the mantle, sliding below another plate(*1*, *2*). The plate interface, or megathrust (Fig. 1), is populated by asperities where the two plates transiently stick together for tens to hundreds of years, until they break and generate a megathrust rupture (*1*). Slow interseismic loading typically produces gradual surface uplift landward of the locked asperities, followed by rapid co- and postseismic motion that mirrors interseismic displacements (*3*). This pattern presumably repeats itself over hundreds of thousands of years as the upper plate experiences countless cycles of loading and unloading. To mitigate the hazard associated with megathrust earthquakes, geodesists routinely measure rates of interseismic surface displacement and invert them for a distribution of slip deficit with respect to the convergence rate along the subduction interface (*4*–*6*). This helps locate locked asperities, also known as highly coupled regions, and evaluate the seismic risk they pose. This approach is inherently limited by the uneven spatial coverage of geodetic data (*7*, *8*), but also by its short temporal span. Specifically, it is unclear whether the spatial pattern of megathrust locking persists or evolves over multiple seismic cycles. Knowing this would provide valuable insight into the physical mechanisms that underlie megathrust locking (*9*).

### Megathrust locking leaves distinct geomorphological footprints

Geomorphological observations, on the other hand, cover time scales of 100's of kyrs that are longer than seismic cycles (100s of years), but shorter than the millions of years over which the geological architecture of subduction margins evolves (*10*). A growing body of work suggests that the spatial pattern of megathrust locking between large earthquakes leaves a distinct footprint in subduction landscapes. For example, locked patches associated with great subduction zone earthquakes are typically overlain by forearc basins (*11*), and associated with negative topography (or gravity) anomalies (*12*), suggesting that regions experiencing interseismic subsidence also undergo long-term subsidence over many cycles (Fig. 1). Closer to the land, the seaward end of the erosive continental shelf (shelf break) commonly overlies the downdip end of fully locked megathrust regions(*13*) (Figs. 1,2A1, 2A3, and 3A2). The shelf break can be regarded as a hinge line that marks the beginning of a landward domain experiencing sustained rock uplift, where new rocks are continually raised into the shallow domain eroded by waves. This pattern of long-term vertical displacement bears similarities with that observed during the interseismic phase of the megathrust cycle (Fig. 1). This resemblance is particularly striking in the Himalayan subduction zone, where the field of rock uplift that has prevailed over the last 100s of kyrs can be inferred from fluvial incision rates (*14*), river profiles (*15*), or changes in valley width (*16*). This field features a broad peak of rapid rock uplift above the downdip end of full megathrust locking (Fig. 2B1). A similar peak exists in the field of ongoing, interseismic vertical displacements measured over decades (*17*, *18*) (Fig. 2B2). Intriguing correlations have also been reported between along-strike changes in subduction morphology and present-day interseismic deformation. In Central and South American subduction zones, the position of peninsulas, for example, coincides with regions of reduced megathrust locking (*19*, *20*). Furthermore, Quaternary uplift rates along the Chilean coast recorded by marine terraces (*21*) systematically amount to 4–8% of present-day interseismic uplift rates (*22*) . Lastly, areas of faster Quaternary uplift are also associated with greater upper-plate seismic activity during the interseismic phase (*23*). These observations hint at a close link between the processes fueling megathrust earthquakes over time scales of decades to centuries and those shaping subduction landscapes over hundreds of thousands of years.

These connections between short- and long-term timescales are often interpreted as manifestations of unbalanced earthquake cycles (*15*, *24–26*), meaning that interseismic and co/post-seismic displacements do not cancel each other, but sum into a poorly-known field of residual interseismic uplift/subsidence that shapes the forearc landscape (*15*, *20*, *27*). This interpretation is, however, at odds with the widely used backslip model (*5*) , which is the standard model for characterizing deformation associated with earthquake cycles (*8*, *22*, *28*, *29*). This framework assumes purely elastic off-fault deformation, such that non-recoverable strain other than slip on the megathrust is not expected, resulting in no long-term rock uplift. We instead propose that increments of non-recoverable, distributed brittle deformation in the upper plate accumulate during the interseismic phase of the megathrust across subduction forearcs, in a manner that is strongly modulated by megathrust locking, and account for most of the geomorphological observations described above.

## From interseismic locking to long-term uplift

Stresses in the brittle forearc must reach certain thresholds for inelastic deformation mechanisms to become activated during the interseismic phase (*30*).It was previously noted (*31*) that down-dip gradients in the degree of megathrust locking are a straightforward way of generating stress concentrations in the upper plate. Furthermore, previous work(*23*, *27*) postulated a link between long-term uplift and upper plate seismicity. Our model integrates these ideas into a workflow that relates short-term locking state to long-term uplift (see Methods). We illustrate it below through the example of the Cascadia, Chile and the Himalayan subduction zones.

### *Summing locking-driven seismicity to explain long-term forearc surface motion*

The current state of locking on a megathrust (Fig. 2A4) can be inferred by inverting geodetically-determined surface displacements within the backslip framework (Fig. 2A2). We use this model to determine the compressive Coulomb stress change imparted by the locking distribution on the forearc wedge, assumed homogeneous (Fig. 2A4). We disregard Coulomb stress changes that drive extensional slip, as we assume the upper plate is near a state of overall compressive yielding (*32*). The largest compressive stress rates occur above the transition zone (Figs 1 and S1) connecting the fully locked and fully slipping portions of the megathrust. This is also the area where seismicity tends to cluster, for instance in the Cascadia forearc (white circles in Fig. 2A4), as revealed by a recent 4-year OBS survey (*33*). We hypothesize that this seismicity is a signature of the upper plate yielding between large megathrust earthquakes, which over longer time scales shortens and thickens the forearc in a coherent, non-reversible manner (Fig. 1). To quantify this deformation, we generate millions of synthetic earthquakes spanning thousands of years and dozens of seismic cycles. We spatially distribute these synthetic earthquakes within the forearc by assuming a linear relationship between Coulomb stress rates and seismicity rates (*34*, *35*) (see Methods). We assign these synthetic events a seismic moment randomly drawn from the locally measured Gutenberg-Richter distribution. Each event is then associated with a rectangular fault patch and a reverse slip vector consistent with empirical moment-displacement scalings (*36*). Fault patches are assumed to have optimal landward or seaward dips with respect to a state of horizontal compression (i.e., dips of ~30º). By adding the elastic displacement fields caused by each individual earthquake (*37*, *38*), we effectively compute the cumulative surface motion resulting from seismicity over thousands of years representing numerous seismic cycles. We postulate that this distributed inelastic forearc deformation cannot be recovered when the megathrust slips and therefore constitutes a reasonable proxy for the long-term uplift field that shapes the landscape.

### ***Application to the Cascadia subduction zone***

To model a 2-D cross-section of the Cascadia subduction zone, we generate 1.9 million synthetic earthquakes distributed spatially according to coupling along the interface (Lindsey et al., 2021) (Fig. 2A4) and the Gutenberg distribution observed by a local seismic catalog (*33*). Considering current seismicity rates in the region (Figs. S3 and S4, text S3), this synthetic catalog covers ~72,000 years, which amounts to ~140 earthquake cycles assuming ~500-year cycles (*39*). The displacement fields of individual forearc earthquakes sum coherently (*40*) into a broad peak of rapid surface uplift located above the locking transition zone (Fig. 2A1). This peak is flanked by a landward zone of subdued uplift, and a seaward region of moderate subsidence. We attribute this pattern to the clustering of thrust events in the region of highest Coulomb stress rates, effectively acting as a deep zone of horizontal shortening that lifts the surface and produces gentle downward motion in the far field. Remarkably, our predicted field of long-term uplift produces a hinge line between seaward subsidence and landward uplift that coincides with the edge of the Cascadia shelf, and the downdip end of the fully locked zone (Figs. 2A1,3), supporting previous interpretation (*13*). Furthermore, the uplift rates we infer are on same order of magnitude as those recorded by marine terraces (*41*) at different distances from the trench (~0.1 mm/yr; Fig. 2A1). We thus suggest that coherent stacking of displacements due to upper-plate seismicity is a viable mechanism to explain long-term deformation of the Cascadia forearc.

### ***Application to the Himalayan and Chilean subduction zones***

We further test our model by applying it to the Himalayan and northern Chilean subduction zones (Figs. S6-S8) where datasets documenting coupling distributions (*22*, *28*), upper plate seismicity (*42*–*44*) , interseismic displacements (*17*, *18*, *22*) and long-term rock uplift (*14*, *21*, *45*) are available. The Himalayan example (Fig 2B) is in many ways similar to Cascadia, where upper plate seismicity clusters where the locking distribution imparts the highest compressive stress rates, i.e., above the locking transition zone (Fig. 2B2). The long-term uplift field computed from 0.5 million synthetic events spanning 2000 years (ten ~200 years long cycles; (*46*)) closely resembles that inferred from river incision rates (*14*), fluvial geometry (*15*), as well as catchment-wide erosion rates (*47*). Specifically, they all involve a broad peak above the locking transition zone at roughly 100 km north of the Main Frontal Thrust, and long-term rates on the order of mm/yr (Fig. 2B1). Our model, however, does not account for rapid rock uplift in the Siwaliks (Fig. 2B), which we attribute to the geometry of the Main Frontal Thrust (*48*) rather than to inelastic interseismic deformation within the upper plate.

In northern Chile, the locking transition zone directly underlies the coastal domain (*22*). Consequently, the surface displacements from 2.9 million synthetic events spanning 17 thousand years (68 cycles assuming ~250-year cycles (*49*)) stack into an uplift field with a broad peak centered on the coast (Figs. 2C1,3), with coastal uplift rates of ~0.5 mm/yr, slightly exceeding the rates inferred from marine terraces (*21*). We further predict a gradual, landward decrease in long-term uplift that is consistent with regional proxies for uplift derived from the topography of the coastal range and the pattern of river incision across it (see Methods; Fig. 2C1). Our expected hinge line between seaward subsidence and coastal uplift, however, lies ~15 km landward of the edge of the narrow continental shelf. We also acknowledge that clusters of forearc seismicity do not exclusively occur in areas where we predict high Coulomb stress rates (Fig. 2C4). Overall, the slight mismatch between our model and geomorphological data suggests that additional mechanisms beyond inelastic deformation induced by locking gradients contribute to the morphology of the Chilean forearc.

## Additional sources of complexity in forearc morphology

Slip on faults of all sizes distributed across the forearc and activated by locking-induced compression is hardly the only inelastic deformation mechanism that can sculpt forearc landscapes. Pressure solution (*50*) and brittle creep (*51*) are other possible ways of permanently straining the upper plate between large earthquakes. Non-recoverable strain may also accrue during megathrust ruptures, in the form of shallow plastic yielding (*52*), shallow fracturing (*53*), broad outer wedge failure (*54*), or fracturing in the damage zone of rupturing asperities (*55*). Whether these mechanisms would imprint a spatially coherent mark in subduction landscapes however remains unclear. Alternatively, processes not directly related to the seismic cycle such as underplating (*56*, *57*) could plausibly result in a local maximum in forearc uplift. Interestingly, underplating requires the development of secondary fault systems above the megathrust that enable the aforementioned mass transfers (*56*). Stress changes caused by locking gradients could well influence the development of such structures, and contribute to the link between seismic cycle deformation and long-term uplift.

Our model also has inherent limitations, which relate to a number of simplifying assumptions. Among them is the treatment of the upper plate as a uniform elastic half-space on the verge of compressional failure. In reality, the forearc may be away from compressional yield with entire regions experiencing horizontal deviatoric tension (*10*, *58*). Repeated failure may also damage and weaken the forearc in a highly heterogeneous fashion that cannot be simply accounted for in our model. Another shortcoming of our approach is that it does not self-consistently predict the absolute magnitude of uplift (only its dimensionless shape). An absolute rate requires knowledge of the Gutenberg–Richter A-value, i.e., the absolute seismicity rates for the region of interest. Improvements of our model would necessitate a rheology-based determination of yielding regions and inelastic strain rates, in a manner that is self-consistent with the stress rates imposed by locking.

## Broader Implications for Subduction Landscapes

In spite of its limitations, our model provides a first-order explanation for the common traits between long-term and interseismic uplift in Cascadia, the Himalayas, and Northern Chile. In order to investigate the broader implications of observed global trends in subduction landscapes, we perform 760 additional model runs, each involving a unique locking distribution, where the extent of the fully locked zone, measured from the trench, spans 30 to 205 km. We examine the dimensionless shape of the long-term uplift field produced by each of them (Figs. 3A1,2). Consistent with our prior results (Fig. 2), the broad peak of long-term uplift systematically overlies the locking transition zone, regardless of its depth, and the hinge line between seaward subsidence and long-term uplift follows the downdip end of the fully locked zone. Our model thereby accounts for the global co-location of the downdip end of locking and shelf breaks (*13*) through the location of the high stress rate area and resulting inelastic strain (Fig. 3A2). The relationship between areas with reduced integrated coupling and the occurrence of peninsulas can be seen as a corollary to this phenomenon (*19, 20*). To illustrate this, we compute the long-term uplift field within a 4000-km long (along-trench) domain that includes a zone of anomalously low integrated coupling, where the locking transition zone is closer to the trench (Figs. 3B2, D). There, the model produces an uplift peak which is closer to the trench and shifts the shelf break and the coast seaward, which could result in a peninsula (Fig. 3B). Conversely, an area prone to large seismic ruptures, i.e., with an extensive locked zone (and a locking transition zone further away from the trench), will tend to subside long-term. Sustained subsidence (Fig. 3B1) over many seismic cycles may contribute to the formation of forearc basins (*11*). Finally, we calculate uplift rate anomalies relative to the cross-trench uplift profile averaged along our entire domain (Fig. 3B1). This yields negative uplift anomalies over regions where full locking extends further downdip of the trench (Figs. 3C1,2), i.e., and may provide an explanation for the negative topography/gravity anomalies reported above the areas of large coseismic ruptures (*12*).

Our model effectively explains the correlation between short-term and long-term deformation in subduction zones and indicates that incremental inelastic interseismic deformation accumulates over multiple seismic cycles, resulting in a long-term strain imbalance, and a coherent landscape signature (Fig. 4). This implies that to first order, the downdip pattern of megathrust locking tends to remain steady over landscape-shaping time scales (100's kyr). If locking were to change frequently, subduction landscapes would integrate a fluctuating field of rock uplift, and the correlation between landscape and geodetically measured rock uplift would be lost. For example, the lumpy bathymetry and absence of striking slope break across the shelf edge at the Japan subduction stands in contrast to the regularity of the continental slope at the Cascadia and Central American subductions, for example. This may illustrate the landscape signature of a shifting uplift pattern derived from frequent changes in megathrust coupling (*13*). Sedimentary series and marine terraces along the coastline of northeast Honshu show persistent subsidence at $10^3$–$10^4$ yr timescales but rock uplift at $>10^5$ yr (*59*, *60*), while the instrumented late interseismic phase records subsidence at the coastline (*26*, *61*). It is conceivable that the alternating deformation recorded in the landscape and its irregular topography directly reflect older coupling configurations that no longer describe the current field interseismic deformation. The patterns of crustal deformation encoded in subduction landscapes over timescales from seconds to hundreds of kyr would, therefore, be an indirect but exploitable proxy for the evolution, stability, or transience of megathrust coupling over geological time, and could be used to evaluate seismic hazard in regions with poor geodetic coverage.

**Acknowledgements**

We are grateful for prolific discussions with Jean-Philippe Avouac, Mark Behn and Roger Buck. We express our gratitude to Benoît Bovy for providing valuable assistance with computational issues.

**Funding:**

Emergence(s) - Ville de Paris Program Project "Inelasticity in the Subduction Earthquake Cycle"(J.-A.O)

European Research Council (ERC) under the European Union's Horizon 2020 research and innovation program ,Geo-4D project, grant agreement 758210. (R.J.)

Institut Universitaire de France (R.J)

H2020 European Research Council, grant no. 803721(BG).

**Author contributions:**

Conceptualization: BO, JAO, RJ, LCM, BL
Methodology: BO, JAO, RJ, LCM
Investigation: BO, JAO, RJ, LCM, BG
Visualization: BO, JAO, LCM
Funding acquisition: JAO
Supervision: JAO, BO, RJ, LCM
Writing – original draft: BO, JAO,LCM,BG
Writing – review & editing: BO, JAO, RJ, LCM, BG, BL

**Competing interests:** Authors declare that they have no competing interests.

**Data and materials availability:**

Seismicity, interseismic, and slip-deficient datasets can be obtained through the original papers referenced in the main text. Geomorphic datasets are found in the OCTOPUS database and in papers presented in the main text. Digital elevation models (DEMs) are accessible through the OpenTopography database. The code used to compute the results is available at https://github.com/baroryan/subductionLandscapes.git

**Supplementary Materials**

Materials and Methods
Figures S1-S11
Supplementary Text S1-S9
Table S1
References (63-92)

**Figures**

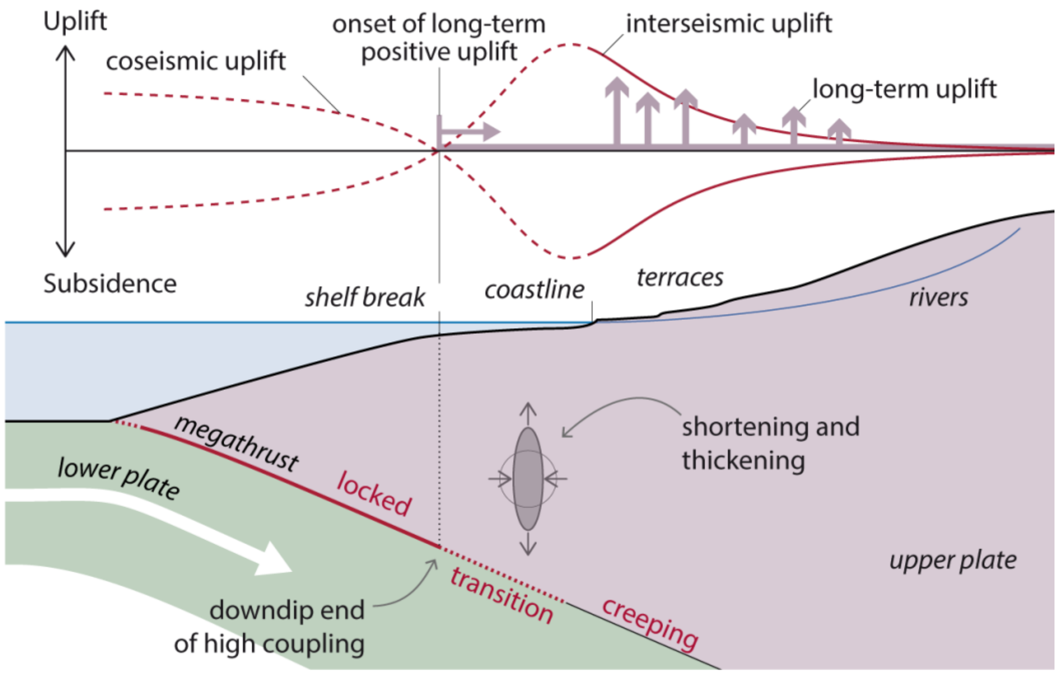


**Figure 1 - Signatures of the short-term megathrust cycle in long-term forearc morphology**. Elastic surface displacement during the interseismic and coseismic periods is denoted by red curves. Evidence for permanent surface deformation recorded by rivers, terraces, and shelf breaks is marked by brown arrows.

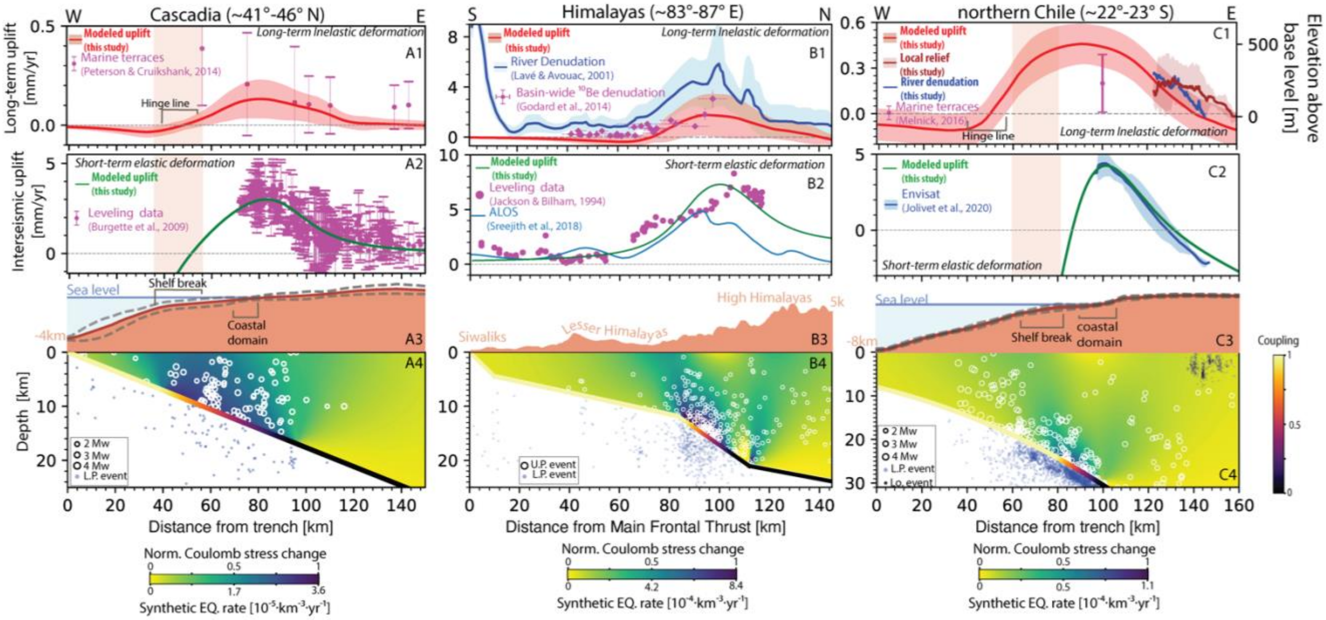


**Figure 2- Short- and long-term uplift at the Cascadia (A), Himalayas (B), and northern Chile (C) subduction zones**. 1 - Long-term uplift computed by our model and recorded by: marine terraces (*21, 41*), basin-wide denudation (*45*) rate, and rivers (*14*). 2 - Interseismic uplift inferred by our models and documented by leveling data (*17*, *62*) and InSAR (*18, 22*). Continuous curves overlapped by light filling denote dataset mean and standard deviation, respectively. Error bars mark one standard deviation. Light brown background marks the position of the shelf break in the swath. 3 - Mean topography of the transect where earthquakes are recorded. Dashed lines denote one standard deviation. (Figs. S3, S5-6 and text S3-4). 4 - Normalized Coulomb stress change and rate of synthetic earthquakes used to compute inelastic uplift. Recorded seismicity is marked by circles (*33*, *42–44*). Subduction zone interfaces are color-coded by the coupling model we used. For a full description of model parameters, see Table S1.U.P.=upper plate. L.P=Lower plate. Lo=Local event.

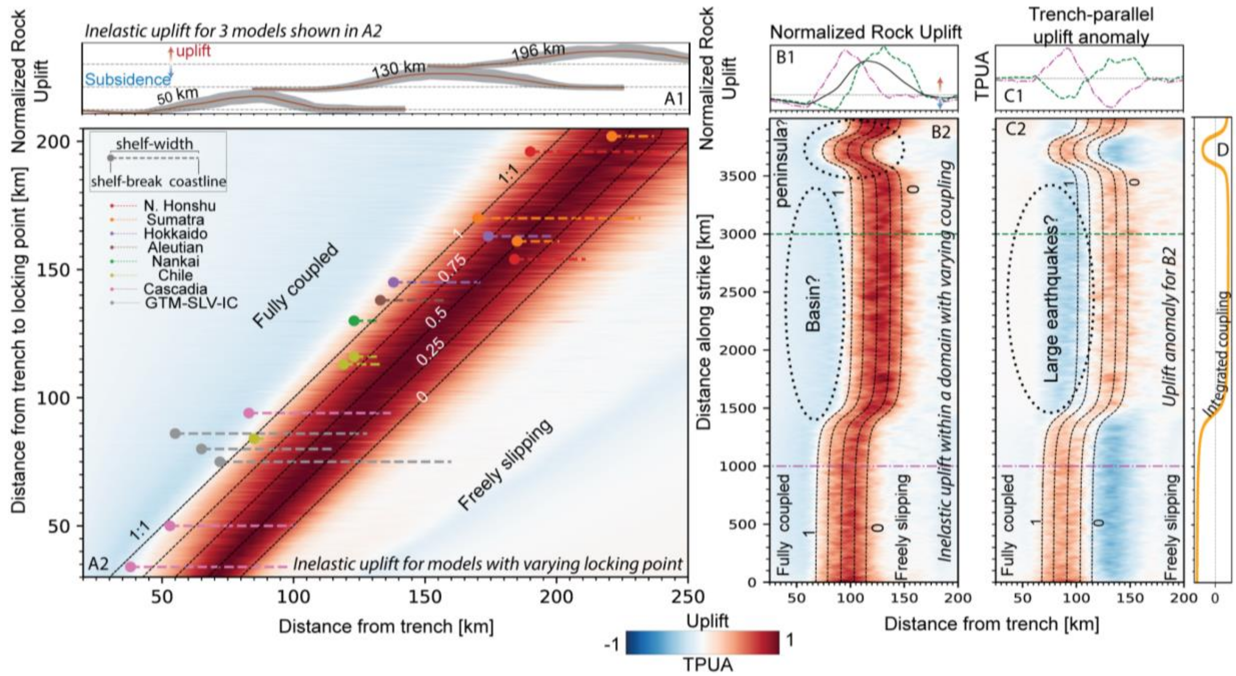


**Figure 3 - Key properties of our predicted fields of long-term uplift.** A2 - Mean inelastic surface uplift for 760 models with varying extents of fully locked zones, spanning a range of 30-205 km from the trench. Each row along the y-axis shows the mean inelastic uplift of a model (color). The mean and standard deviation of uplift are displayed in A1 for three different models. The documented positions of the shelf-break and coastline in a number of forearcs are marked by circles and adjacent lines, respectively (*13*). B2 - Inelastic uplift along a 4000km long domain with varying coupling. B1 - Green and Magenta curves show the uplift along two lines shown in B2. Black line shows the trench-parallel average uplift along the domain. C2 - Trench-parallel uplift anomaly (TPUA). C1 - Green and magenta curves mark the TPUA along two lines shown in C2. D- Integrated coupling along strike for B2 and C2. Thin dashed lines mark the coupling used in computing uplift shown in A2 & B2. For a complete description of model parameters see Table S1.

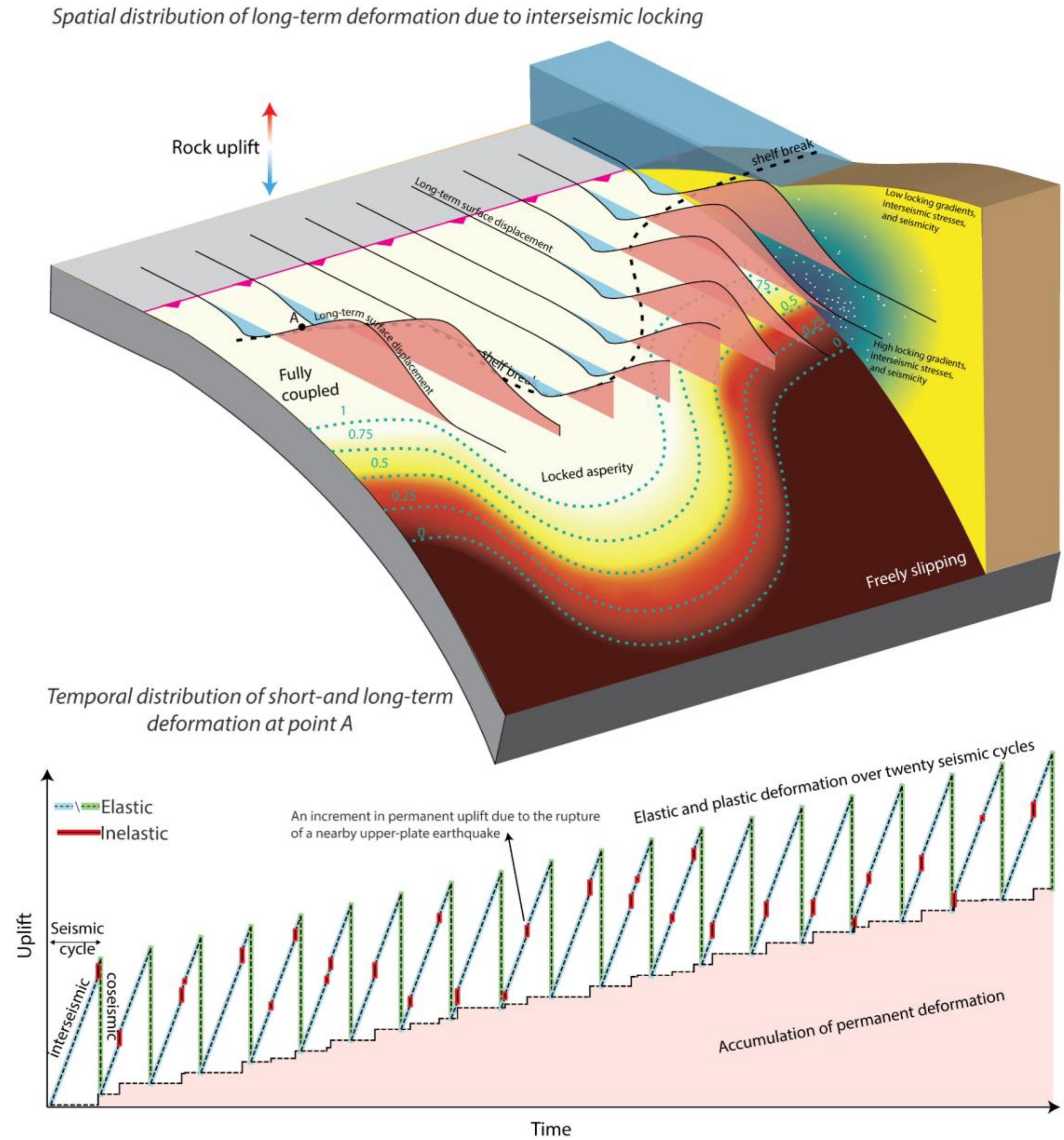


Figure 4 - **Illustration of megathrust locking imprinting subduction zone landscapes over many earthquake cycles.** Upper panel shows the spatial pattern of non-recoverable deformation due to a coupling distribution along a subduction interface. White circles mark upper plate interseismic seismicity activated by locking gradients. The total rock uplift from upper plate earthquakes over many seismic cycles is depicted by 2D plots above the surface. Lower panel illustrates elastic and non-recoverable deformation at point A during twenty seismic cycles.

Science
AAAS

# Supplementary information for

# Megathrust locking encoded in subduction landscapes

Oryan, B., Olive, J.-A., Jolivet, R., Malatesta, L. C., Gailleton, B, and Bruhat, L.

Corresponding author: bar.oryan@columbia.edu

**The PDF file includes:**

1. Materials and Methods
2. Figures S1-S11
3. Text S1-S9
4. Table S1
5. References (63-92)

## Methods

*Interseismic seismicity in the forearc wedge*

To model the distribution of seismicity throughout the forearc wedge we adopt a framework developed by Dieterich (*34*, *35*). This approach combines rate-and-state friction, fault mechanics, and statistical seismology to establish a constitutive relationship between stressing history and seismicity rate. It treats seismicity as a sequence of earthquake nucleation events adhering to time and stress-dependent, rate-and-state equations which characterize unstable slip. This framework has been widely used to describe the spatial and temporal distribution of seismicity that arises from changes in stress and stress rate, and can thus be used to model aftershocks (*35*, *63*–*66*), tidal earthquake triggering (*67*, *68*), earthquake probabilities (*69*, *70*), and induced seismicity (*71*–*75*).

Under the above assumptions, R, the rate of seismicity, writes (*34*, *35*) :

$$1. \quad R = \frac{r}{\dot{S}_b\,\gamma}; \dot{\gamma} = \frac{1-\gamma\dot{S}}{a\sigma}$$

where $r$ is the background rate of seismicity, $\dot{S}_b$ is the background stress rate, $\gamma$ is the seismicity state variable, and $S$ is the modified Coulomb stress:

$$2. \quad S = \tau + (\mu - \alpha)\sigma$$

In equations (1) and (2), $\alpha$ and $a$ are rate-and-state parameters relating changes in normal stress to friction, and instantaneous slip rate to friction, respectively. $\sigma$ and $\tau$ are the normal and shear stress acting on a population of earthquake sources and $\mu$ is the static friction coefficient.

At steady state, $\gamma$ evolves to $\gamma_{ss} = \frac{1}{\dot{S}}$ . It follows that the seismicity rate is proportional to :

$$3. \quad R_{ss} = \frac{r}{\dot{S}_b}\dot{S}$$

Assuming that the entire forearc wedge is under a constant background stressing rate $\dot{s}_b$ that yields a constant seismicity rate, $r$ , we can estimate the perturbed seismicity rate during the interseismic period at every point in the wedge by assessing the modified Coulomb stress change there:

$$4. \quad R_{ss}(x,z) \propto S(x,z)$$

*Coulomb stress change across the forearc wedge*

We consider a forearc wedge underlain by a megathrust in a homogeneous elastic half-space (Fig. S1). We employ the backslip (*5*) and Okada solution (*37*, *38*) and calculate the interseismic strain in the forearc using planar dislocations that slip according to published slip deficit distributions along the megathrust interface (*8*, *22*, *28*). We use these geodetically-derived slip deficit maps to determine where along the interface the coupling transitions from (1) coupled to partially slipping and further downdip to (2) freely slipping.

We model the transition in slip rate between these two points by paving the interface with 100 rectangular dislocations whose slip varies linearly with downdip distance. We neglect 3D variations in coupling and extend these dislocations to a thousand kilometers in the along-strike direction. We also assume that the megathrust interface up-dip of point (1) is fully coupled due to the stress shadowing effect (*8*, *76*). We link strain and stress using Hooke's law, assuming a shear modulus and Poisson's ratio of *30* GPa and *0.25*, respectively. This yields the interseismic Cauchy stress tensor at each point in the forearc wedge, which we use to compute the Coulomb stress change throughout the forearc, assuming receiver faults with dips of 30º.

*Permanent surface displacement from interseismic seismicity*

We estimate the surface displacement from upper plate interseismic seismicity by generating a synthetic earthquake catalog that represents multiple earthquake cycles and compute the associated surface displacements. We neglect lower plate seismicity due to its minor contribution to surface displacement (Text S8 and Fig. S11).

We calculate the Gutenberg-Richter distribution (*77*) for Cascadia, Chile, and the Himalayas by fitting the moment magnitude distribution of local seismic catalogs (*33*, *44*) and previous estimates of the local seismicity (*78*), and generate a random sequence of synthetic earthquakes whose magnitudes comply with the estimated *b* value (See Text S3-S5; Figs. S3-7). We position the hypocenters of these synthetic events within a 3D domain so their location corresponds to the spatial distribution of seismicity according to equation 4. We do so using a sampling rejection algorithm, retaining earthquakes that occur at a random depth, z, and distance from the trench, x only if:

$$5. \quad g(x,z) > u_o$$

Where $u_0$ is a random number uniformly distributed between 0 and 1 and *g(x,z)* is:

$$6. \quad g(x,z) = \frac{S_N(x,z)}{\int_c^1 S_N(x,z)}$$

In equation (6), $S_N(x,z)$ is the modified Coulomb stress (equation 2) normalized with respect to the maximum modified Coulomb stress in the domain. We reduce computation time by limiting our randomly seeded hypocenters (x,z) to a possible nucleation region where $S_N$ exceeds a small threshold *c* of 5% (See text S7 and Figs. S9-10 for verification of model parameters). The along-strike position of these events is uniformly distributed within the domain.

We compute the surface displacement imparted by the rupture of all the synthetic events by assuming they occur on rectangular faults. This is achieved using the Okada dislocation model (*37*, *38*), and empirically-derived relations between moment magnitude ($M_w$), along-strike rupture length ($L_r$), and downdip extent $D_r$ to determine the rupture area A $(= L_r \cdot D_r)$ for each event (*36*):

$$7.\quad L_r = 10^{\frac{M_W - 4.38}{1.49}}; D_r = 10^{\frac{M_W - 4.06}{2.25}}$$

The events' slip ($s$) is then obtained from its seismic moment as:

$$8.\quad s = \frac{10^{1.5M_W - 9.05}}{A \cdot G}$$

Where $G$ is the shear modulus. We consider that events nucleate on 30º-dipping thrust faults (Fig. S1), which are equally likely to dip toward the trench (seaward) or away from it (landward). We assume earthquakes rupture updip from our guessed hypocenter and reject earthquakes whose updip rupture length extends below the megathrust or above the surface. We also impose that earthquakes are 95% less likely to rupture within the shallowest 2 km of the forearc, in accordance with the lack of shallow seismicity observed globally in this depth range (*9*).

We continue to generate synthetic events and sum their imparted surface displacements in an iterative fashion until the standard deviation of the modeled uplift is lower than the average uplift. Effectively, we generate synthetic events until:

$$9.\quad \frac{\sigma_v^{max}(x)}{v_{mean}(x)} < c_0$$

Where $v_{mean}(x)$ is the cumulative vertical displacement averaged along strike measured at distance x from the trench (Fig. S1), $\sigma_v^{max}(x)$ is the maximum along-strike standard deviation of the cumulative vertical displacement, and $c_0$ is a threshold set to 0.2. We convert rock uplift to uplift rate by dividing the cumulative vertical displacement by the recurrence time of the randomly seeded earthquakes, which we infer from the *a*-value of the Gutenberg-Richter distribution (see text S9).

It is important to note that we limit the maximum magnitude according to the largest $D_l$ capable of fitting in the nucleation zone (Fig. S1), and set the minimum magnitude to 4 as smaller earthquakes produce negligible surface displacement (Text S2;Fig. S2) for the *b* values typically measured in convergent contexts (*79*). Finally, we determine the along-strike extent of the domain according to the maximum earthquake length (Fig. S1). For cases where we vary the locking distance from the fault systematically (e.g., Fig. 3A) we set the *b* value to 0.9 according to a global complication of thrust events (*79*). As we are only interested in the spatial pattern of the uplift profile in these cases, we normalize the surface uplift with respect to the maximum value when averaged along strike. For the case shown in Fig. 3C we compute the location of synthetic earthquakes along 800 5 km-long domains with varying coupling and then compute the surface displacement imparted by earthquakes registered in all domains along a 4000 km-long region.

*Northern Chile long-term uplift shape derived from topography and river incision*

The coastal region of northern Chile (~18°-25° S) is an extremely arid region with precipitation rates well below 100 mm/year (*80*). The main rivers flow from the Andes and dissect the landscape of the coastal range during rare extreme flooding events (*81*). The coastal range catchments are often perched above the traversing channels and have very low basin-averaged denudation rates (<0.05 mm/yrs) suggesting that the equilibration time of these tributary river networks is well over millions of years (*80*, *82*, *83*). This very slow response time, combined with an extreme-event-dominated incision limits the use of the fluvial landscape to estimate long-term uplift signature with traditional tools such as channel steepness and the stream power incision (*15*, *84*). Fortunately, the presence of the larger Andean rivers crossing the arid coastal range allows us to use the difference between these river profiles and the uplifted and warped topography as a proxy for the regional uplift pattern.

To do so, we focus our analysis south of the outlet of Rio Loa (21°25' S), one of the few mainland rivers connected to the ocean in Northern Chile. This region is characterized by fairly uniform lithology (*85*) so changes in river incision and surface elevation cannot be attributed to variations in rock erodibility. We use lsdtopytools flow routines (*86*) to extract the main river channel from ALOS World 30m digital elevation model (*87*) and analyze its profile. We constrain incision along the river by measuring the relief between the river bed and the incised surface flanking the canyon in a 1.5 km window across the flow direction (Fig. 2C1). Local relief increases sharply in the immediate proximity of the river and barely changes beyond the canyon walls. This supports the hypothesis that (i) recent river incision does not shape the landscape beyond the river valley, (ii) the river transports the sediment flux to the ocean without intermediate deposition over large areas, and (iii) the uplifted surface can be used as a passive strain marker. Furthermore, we extract a 120 km wide W-E topographic swath profile, south of the Rio Loa where its influence is negligible. We employ the variation in elevation along the swath profile, measured from a base level situated at a plateau between the coastal range and the cordillera, as a second indicator for uplift. The resemblance between the two independent measurements supports the use of the regional topography as a proxy for long-term uplift.

**Text S1 - Domain setup:**

Please see the figure below for an illustration of our model setup. Please note that the domain surface uplift and mean along strike uplift field are examples of what an uplift field might look like.

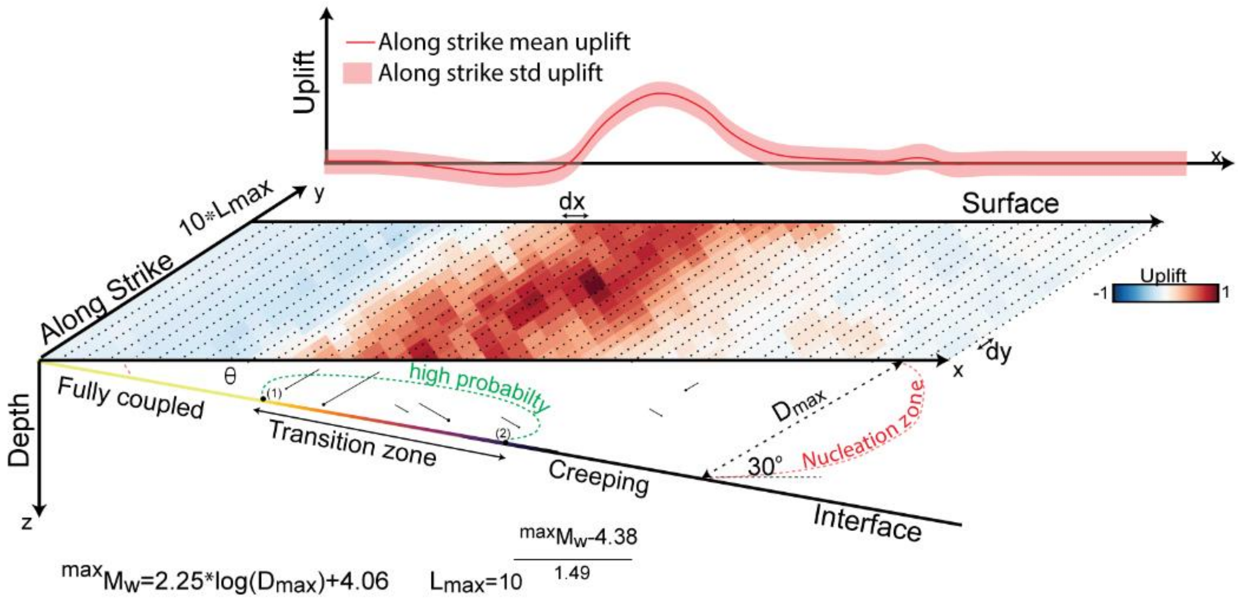


**Figure S1 - Illustration of domain dimensions, synthetic earthquake maximum rupture properties, and model setup and results**. Nucleation region denotes the area where synthetic earthquakes are first guessed and correspond to where $S_N$ (See equation 6) exceeds a small threshold c. High probability zone marks a region where synthetic earthquake density is high, and most surface displacement is concentrated. Dots and adjacent lines mark nucleation points and faults on which earthquakes rupture. Dots on the surface show positions where we compute surface displacement and are color-coded by an example uplift field. $D_{max}$, $^{max}M_w$ and $L_{max}$ are the synthetic earthquake maximum values for the following (1) along dip rupture length (2) moment magnitude and, (3) along strike rupture length, respectively. The interface is color-coded by its coupling.

**Text S2 - Sampling the Gutenberg Richter distribution**

The moment magnitude of synthetic events is drawn from the truncated Gutenberg Richter distribution (*88*) given a certain b value and maximum and minimum event sizes. The upper limit for event size is set according to the dimension of the forearc (Fig. S1), and the minimum size is set due to computational constraints. For typical b values (~0.9-1) small events do not generate substantial surface displacement but pose a considerable computational task. This point is illustrated below, where uplift drawn from the Gutenberg Richter distribution using b value of 0.9 generate self-similar uplift pattern (Fig. S2B) and the total uplift from Mw>3 is essentially identical to events Mw>4 (Fig. S3A). Therefore, we use a minimum event size of 4 in the manuscript.

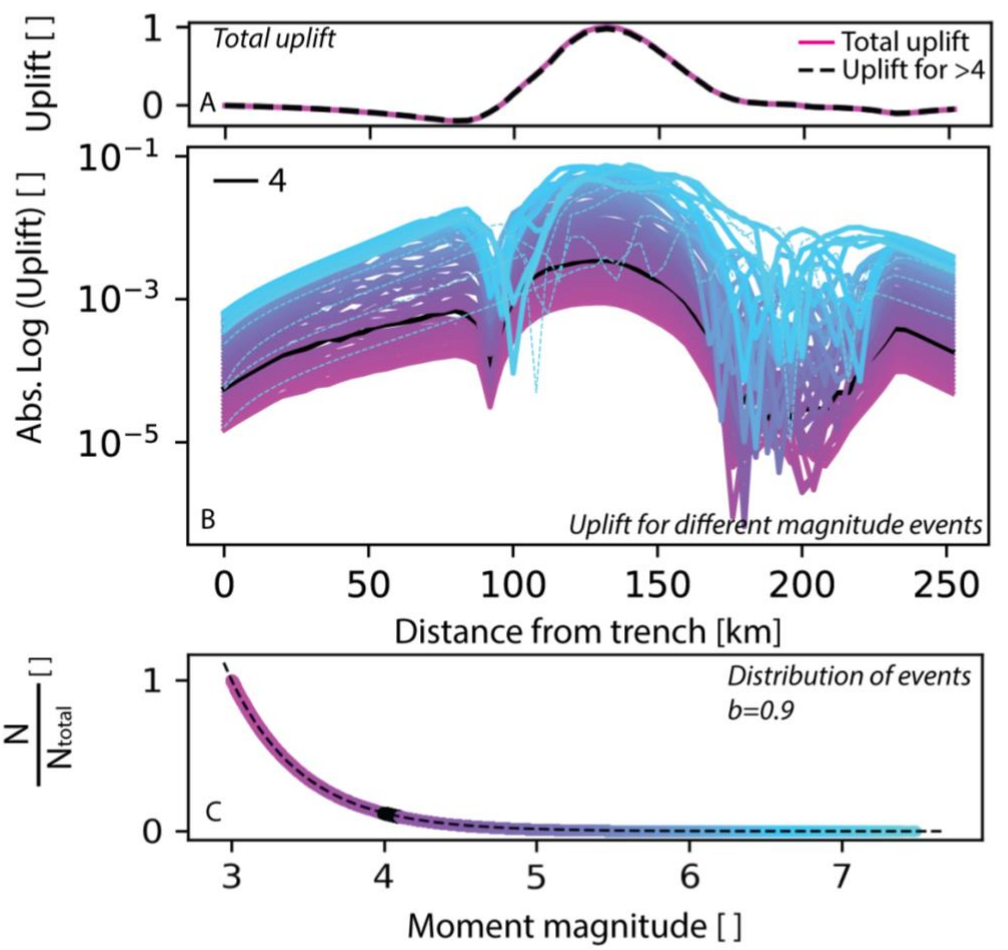


**Figure S2 - Inelastic surface uplift for various earthquake magnitudes.** A - Magenta and dashed black lines show the along strike normalized mean uplift for all and larger than 4 Mw earthquakes, respectively. B - Uplift for events grouped by their magnitude illustrated by the colors shown in panel C. Uplift for magnitude >7 and magnitude 4 events are marked with a thin dash and a black line, respectively. C - Earthquake magnitudes populated in the domain for a random sample of the truncated Gutenberg Richter distribution where b=0.9 and the minimum and maximum magnitude are 3 and 7.5, respectively (see Figure S1). For a full description of model parameters, see Table S1.

**Text S3 - Cascadia**

Our study specifically targeted the southern and central sections of the Cascadia subduction zone, where there is extensive coverage of local seismicity (*33*) and available datasets on interseismic uplift (Fig. S5). To exclude the effects of along-strike 3D changes in the subduction zone geometry and slow slip events, we chose not to extend our transect into the northern section of the Cascadia subduction zone. We used the reported Richter's local magnitude in the catalog we employed (*33*) and estimated the moment magnitude (*89*).We then fitted a and b values assuming a Gutenberg Richter distribution using the least square method (Fig S6). We only consider seismicity recorded in the upper plate and note that the less-than-optimal fit is due to the rolling nature of the deployment of the OBS array (*33*). We would like to highlight that we only use a local catalog recorded by an array of ocean-bottom seismometers (OBS) as we are interested in the precise position of microseismicity offshore. Finally, the long-term uplift uncertainty (Fig. 2A1) stems from both the standard deviation produced by our model and the uncertainty produced by the fit (Fig. S4).

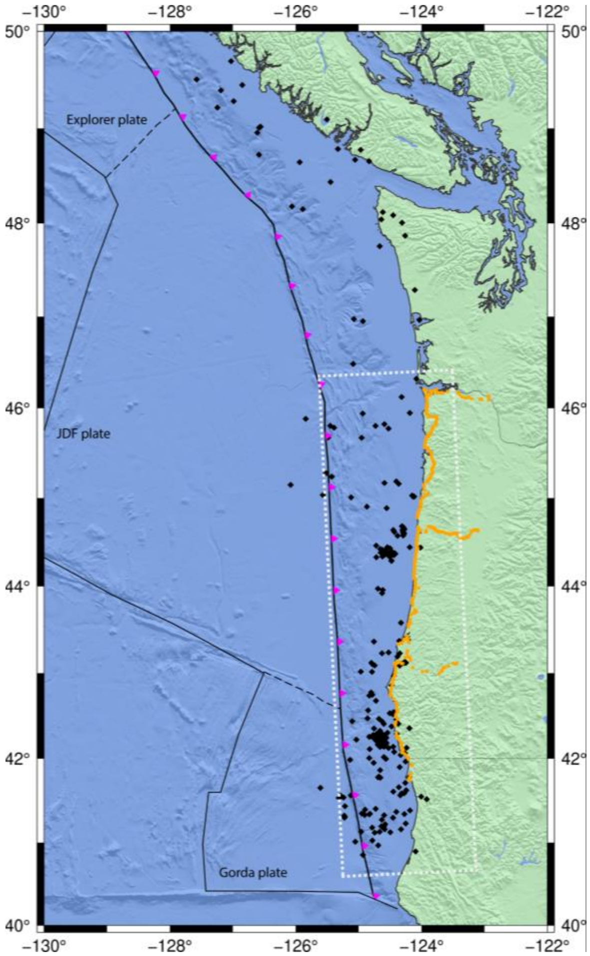


**Figure S3 - Map of data used for the Cascadia case**. Black diamonds mark recorded seismicity (*33*). Orange dots represent the position of leveling data (*62*). Black line with magenta triangles shows the location of the trench. Dash white rectangle denotes the cross-section shown in Fig 2.

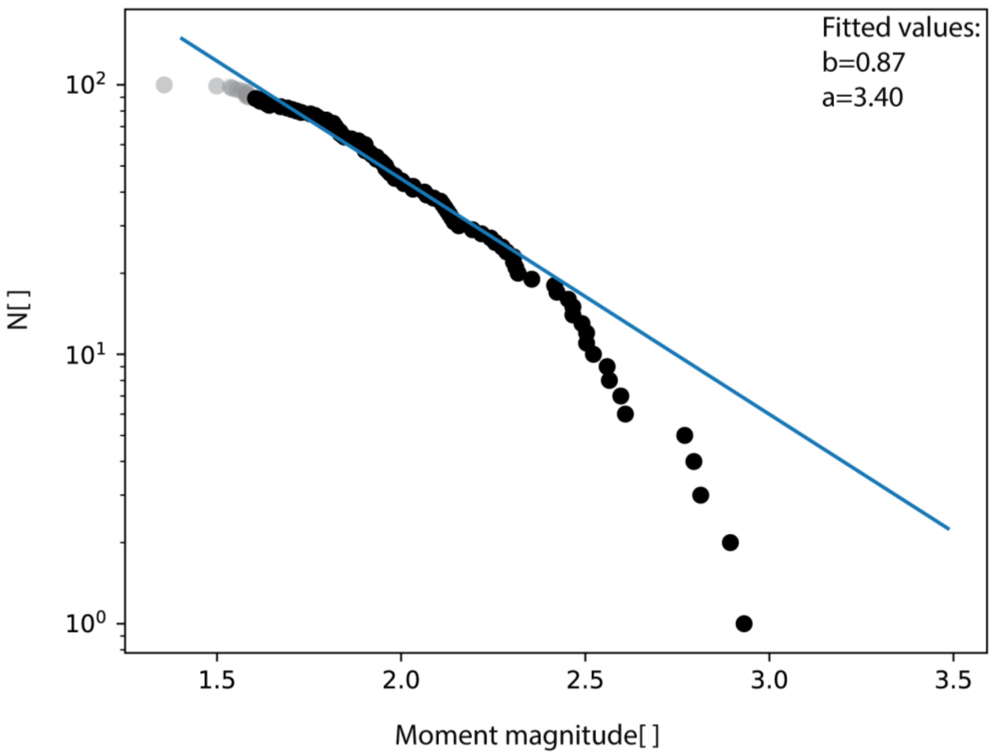


**Figure S4 -Upper plate seismicity** (*33*) **used to constrain a and b values.** Grey and black circles represent events below and above the estimated completeness magnitude, respectively. Only the latter events were used in fitting the data. The blue curve marks the Gutenberg Richter distribution corresponding to the fitted a and b parameters.

**Text S4 - Himalayas**

We focused on the central section of the Himalayas, where ample evidence for interseismic deformation and long-term uplift exists. Our region of interest is characterized by a and b values of -5.3 (km$^2$yr$^{-1}$) and 1.06, respectively (*78*). As we are only interested in upper plate seismicity, we account for the ratio of upper plate events (*42*, *43*) to the total seismicity observed in our transect (Fig. 2B4). This ratio is similar to earlier estimations observed between the productivity along the Main Himalayan Thrust and off-interface seismicity (*90*, *91*). Finally, our long-term uplift uncertainty (Fig. 2B1) is the sum of the standard deviation produced by our model and the uncertainty in a-value (*90*).

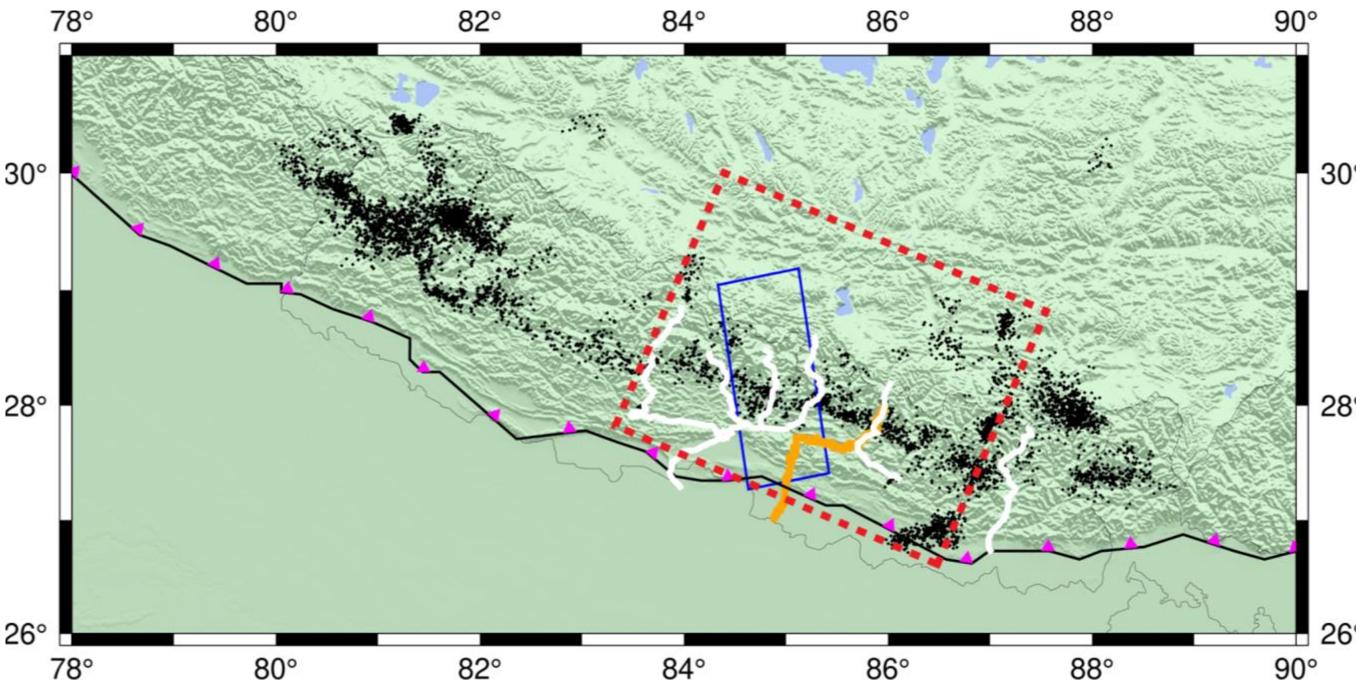


**Figure S5 - Map of data used for the Himalayas case.** Black points mark recorded (*42*, *43*). Orange line and blue rectangle show leveling data transect (*17*) and ALOS track (*18*), respectively. White curves denote rivers used to constrain fluvial incision rates(*14*). Red dash rectangle denotes the cross-section area (Fig. 2B4). Black line with magenta triangles shows the location of the Main Himalayan Thrust.

## Text S5 - Chile

We targeted a region in northern Chile where seismicity is not predominantly linked to specific faults as further north shallow seismic activity is associated with the Adamito Fault (*44*). We used the reported local magnitude in the catalog (*44*) and converted it to moment magnitude (*89*). We then fitted a and b values assuming a Gutenberg Richter distribution using the least square method (Fig S7).

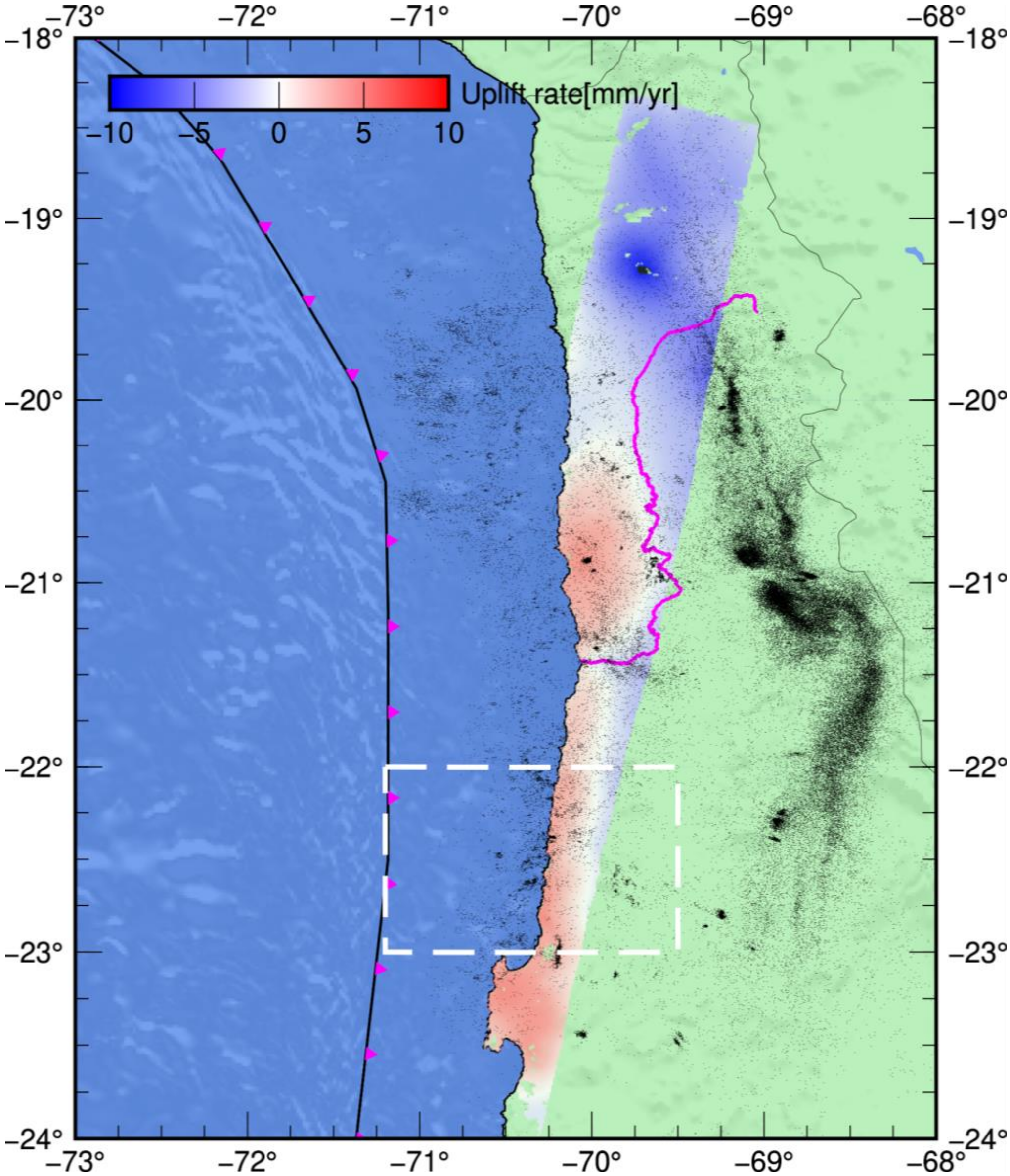


**Figure S6 - Map of data used for the northern Chile case.** Black points mark recorded seismicity (*44*). Intersesismic uplift rates recorded by Envisat are shown by blue and red colors (*22*). Magenta curve denotes the river used to constrain the uplift shape(See method section). White dash rectangle denotes the area of the cross-section (Fig. 2C4). Black line with magenta triangles shows the location of the trench.

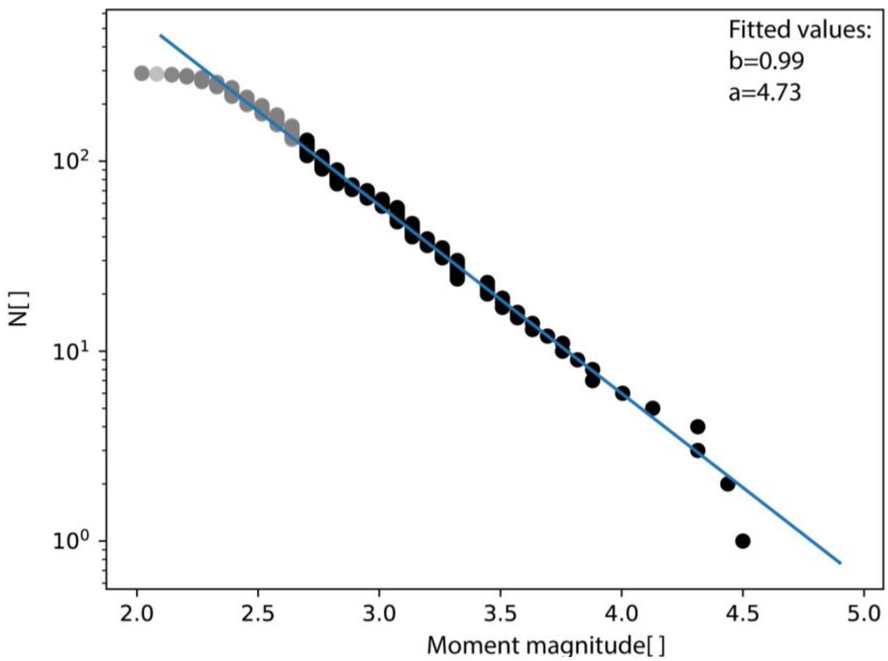


**Figure S7 - Upper plate seismicity** (*44*) **used to constrain a and b values.** Grey and black circles represent events below and above the estimated completeness magnitude, respectively. Only the latter events were used in fitting the data. The blue curve marks the Gutenberg Richter distribution corresponding to the fitted a and b parameters.

**<u>Text S6 - Agreement between our model and recorded seismicity</u>**

We compare the spatial distribution of recorded seismicity in Cascadia, Himalayas and northern Chile with generated synthetic events derived by our method (eq. 6). For reference, we also include events that are uniformly distributed within the forearc.

To capture the variability in the recorded seismicity, we assume a 5km uncertainty in the position of documented events and sample 1000 occurrences for each earthquake, considering a normal distribution. We emphasize that seismic activity in northern Chile and Cascadia is limited due to the arrangement of seismometers used to capture these events. In Cascadia, on-shore seismicity is missing due to the OBS array located off-shore, while in Chile, events close to the trench are absent due to the position of the land-based array. Nonetheless, given these limitations and the fact that recorded seismicity is documented in a time span of a few years, merely a fraction of one interseismic period suggests a good correlation with our synthetic events (Fig S8), particularly along the x-axis where peak seismicity coincides nicely.

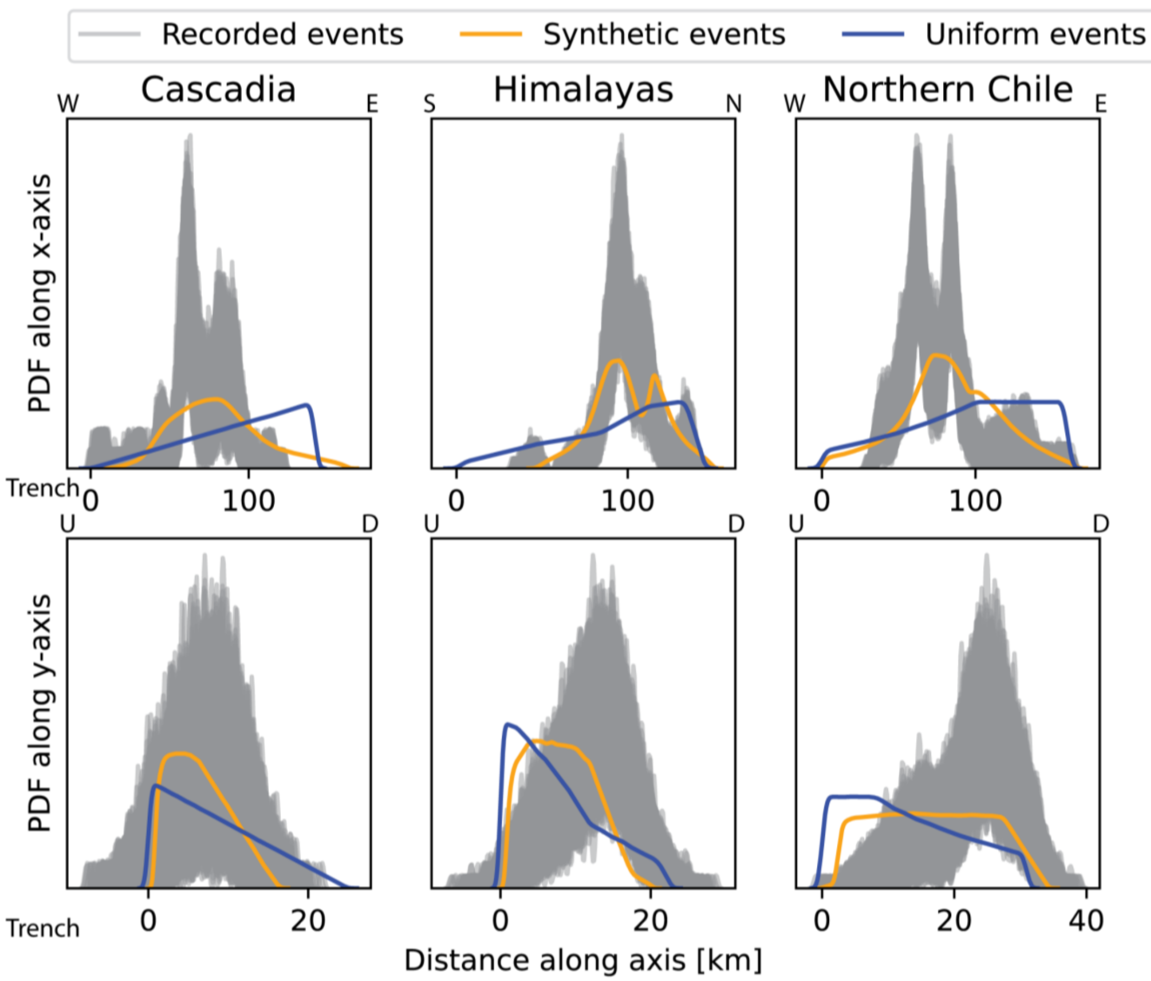


**Figure S8 - Comparison between synthetic events (Eq. 6; orange), uniform distribution events (blue), and upper plate seismicity** (*33*, *42*–*44*)**.** Each gray line corresponds to one sample generated from the normal distribution. The orange and blue curves correspond to the PDF derived from 1 million events.

**Text S7 - Verification of model parameters**

We conducted an extensive exploration of model parameters to assess the robustness of our key findings. Firstly, we investigated the impact of varying the width of the transition zone on the pattern of inelastic uplift. As anticipated, the location of the hinge line remained relatively constant, while the width of the inelastic uplift zone exhibited a correlation with the width of the elastic transition zone (Fig. S9A). When testing the effect of the dip angle, we observed that larger dip angle values resulted in the hinge line moving closer to the trench and the inelastic uplift zone widens (Fig. S7C). This is likely the result of the interaction between the dip angle, free surface, and locking gradeints stresses. Next, we systematically adjusted the cutoff parameter (c in eq. 6) and observed that while the hinge line remained stationary, the width of the uplift zone decreased with larger cutoff values (Figs. S9B & S10). This is attributed to synthetic earthquakes and resulting deformation concentrated in the region of the highest stresses near the downdip end of the coupled zone.

It is interesting to note that increasing the cutoff parameter is similar to assuming that large regions of the upper plate are far from compressional yield. As can be seen in Figs. S9B and S10, this does not fundamentally alter our results, as we still maintain a strong hinge line with a pronounced permanent uplift region. This suggests that as long as a small part of the upper plate is in compression, a characteristic landscape (as described in the main text) will be produced.

Lastly, varying the alpha parameter, which is the least constrained in our model, showed minimal impact on the width of the uplift zone, and the position of the hinge line remained largely constant (Fig. S9D).

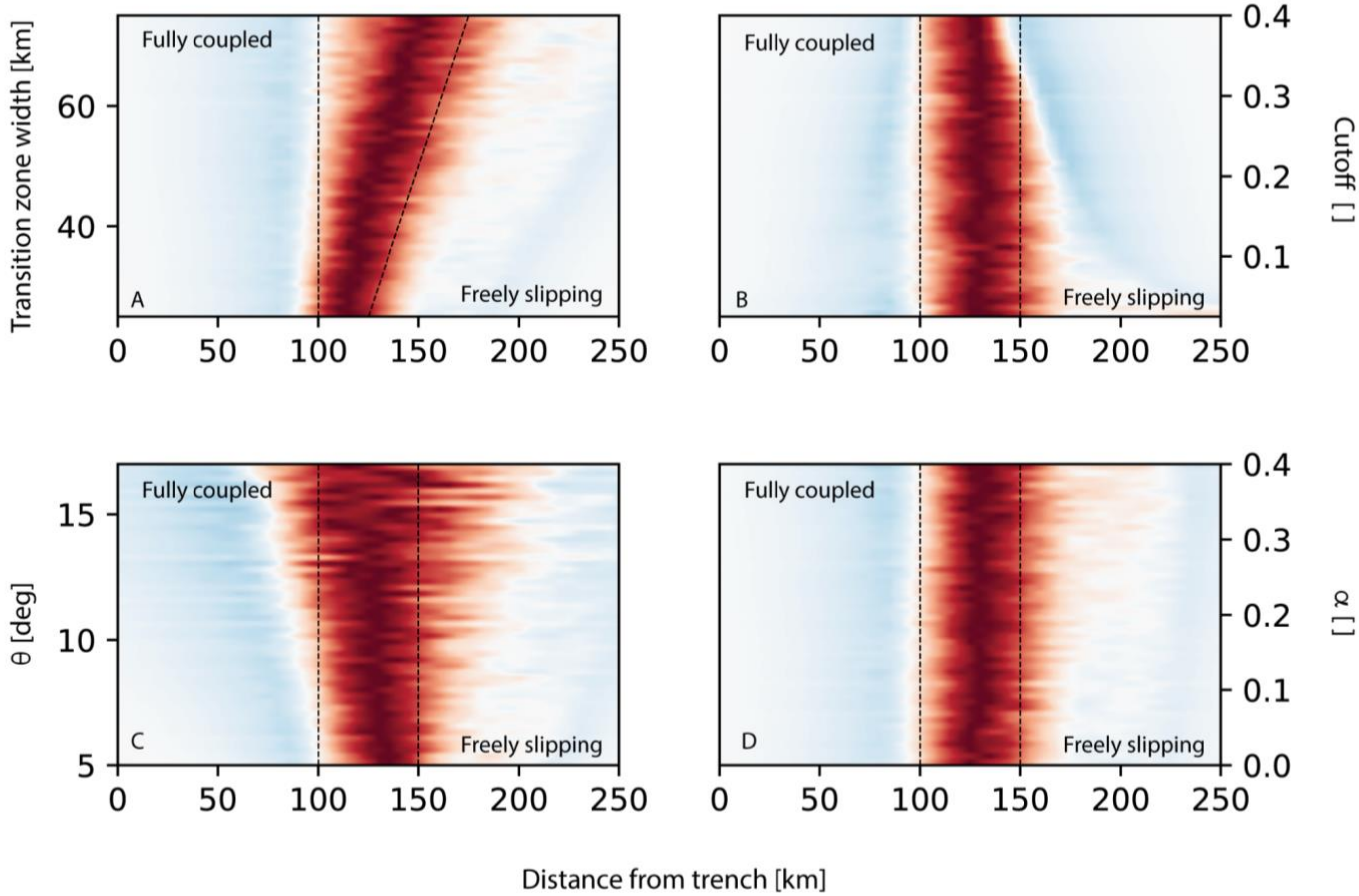


**Figure S9 – Long-term uplift for different parameters.** Dash thin lines mark the transition in coupling. For a full description of model parameters, see Table S1.

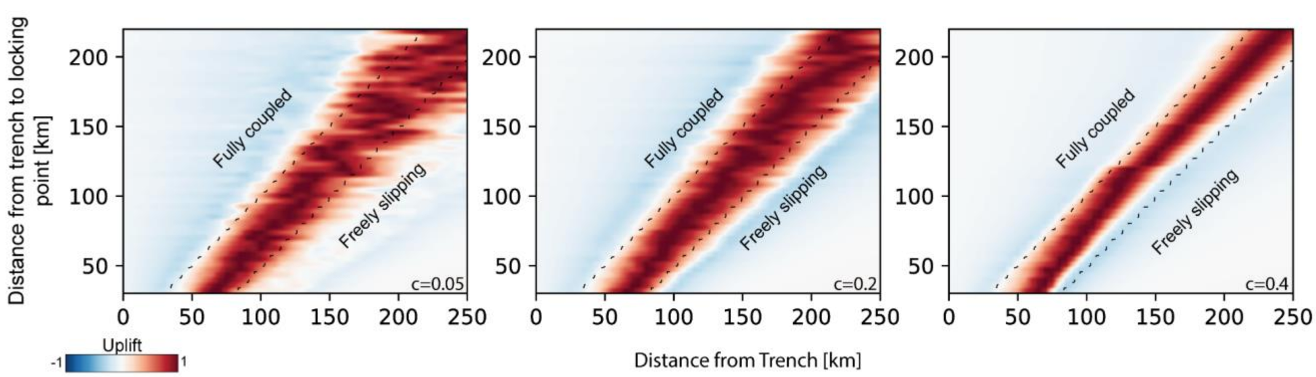


**Figure S10 - Mean surface inelastic uplift for varying cut-off parameters.** Dash thin lines mark the transition in coupling. For a full description of model parameters, see Table S1.

**Text S8 -The contribution of an inelastic lower plate on long-term surface uplift**

To reduce computation time, we ignored the contribution of inelasticity in the lower plate (LP) even though LP earthquakes are documented in close proximity to the down dip end of the fully coupled zone (Figs. 2A4,2B4 & 2C4). Here we demonstrate that the effect of LP seismicity resulting from locking gradients on surface deformation is negligible. We consider a forearc fully locked for a distance of 100km and assume that the background stress state of the LP and upper plate (UP) is extensional (*10*) and compressional, respectively. We compute the extensional coulomb stress change in the LP and the compressional coulomb stress change in the UP (Fig S11B), and populate the plates with synthetic earthquakes according to equation 6. We consider LP and UP earthquakes to nucleate on 60º-dipping normal faults and 30º-dipping thrust faults, respectively. These events are equally likely to dip toward the trench (seaward) or away from it (landward).

We sum the surface displacement of these synthetic events and observe that the depth at which LP earthquakes occur limits their influence on the surface. This leads to a relatively modest LP long-term displacement, which is minor in comparison to the contribution of shallower UP thrust events (Fig. S11A). We highlight that while this analysis examines a specific coupling configuration, it points to a border phenomenon demonstrating that down-going inelastic seismicity resulting from locking gradients has a small effect on the surface.

Finally, for completeness, we also show that assuming a compressional LP (Fig. S11C) results in an even smaller long-term uplift concentrated in the vicinity of the trench, having no real impact on the principal uplift field situated above the transition zone (Fig. S11A).

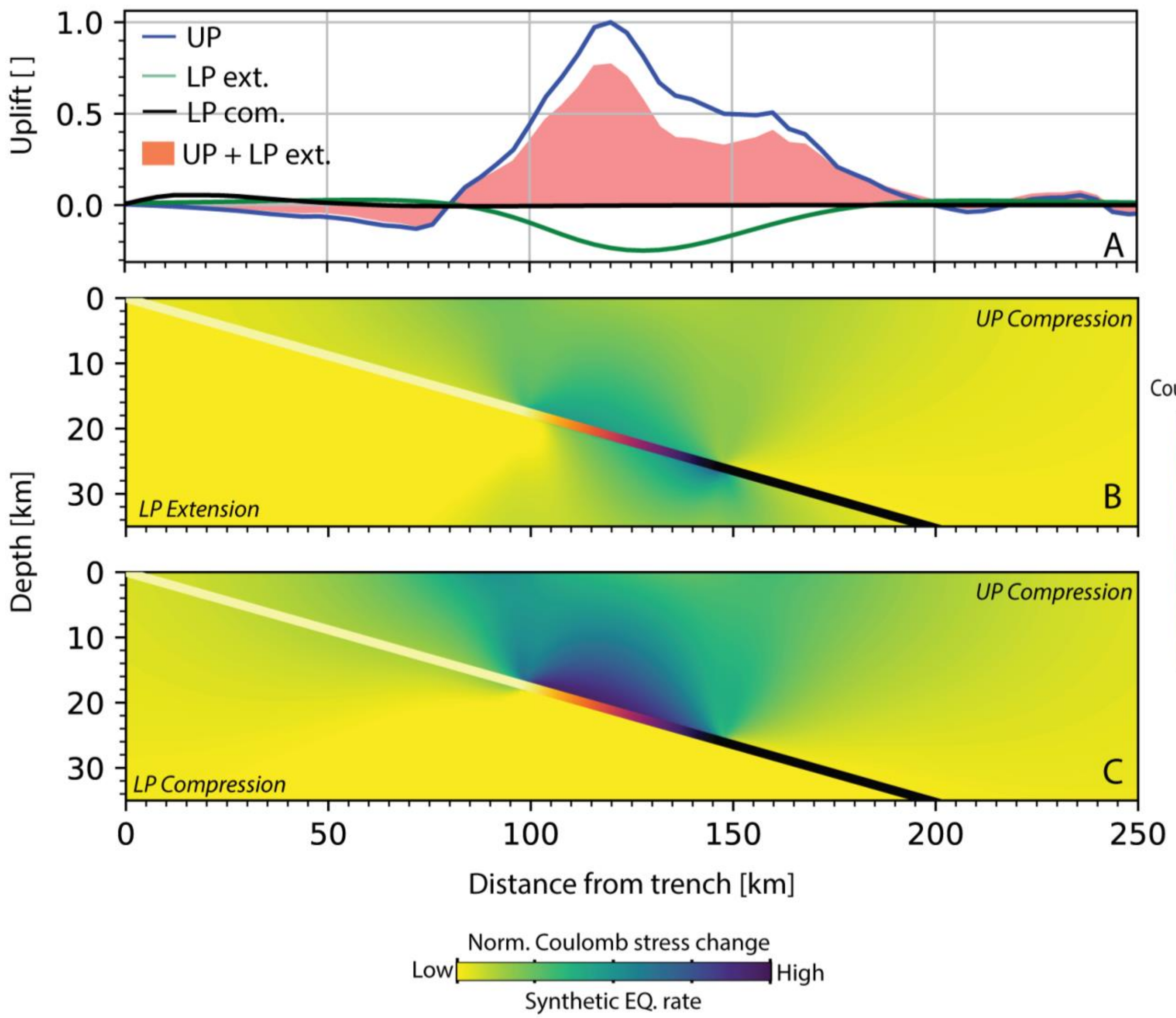


**Figure S11 - Contribution of LP yield on permanent surface displacement.** A - Uplift from compressional and extensional UP and LP. B - Normalized UP Compressional and LP extensional coulomb stress change. C - Normalized UP and LP Compressional and coulomb stress change. Coulomb stress change values are normalized with respect to the largest absolute value in the domain. The interface is color-coded by the coupling model used. For a full description of model parameters, see Table S1.

**Text S9 - Converting long-term surface uplift to uplift rate**

Seismicity is recorded in a given forearc within a surface area $A_f$ during time T, yielding Gutenberg Richter distribution with a and b values. The number of earthquakes larger than $M_w$ 4 during a certain unit of time and area is $N_f$:

$$N_f = \frac{10^{a-4b}}{T \cdot A_f}$$

Using our model, we compute the long-term surface displacement ,$U(x,y)$, within a domain with a surface area $A_d$ resulting from $N_d$ synthetic events randomly sampled from a Gutenberg Richter distribution with the same measured forearc b-value. The uplift rate, $V_u(x,y)$, is then:

$$V_u(x,y) = U(x,y) \cdot \ N_f / \frac{N_d}{A_d} = U(x,y) \cdot \frac{10^{a-4b} \cdot A_d}{A_f \cdot T \cdot N_d}$$

Where x and y is distance from the trench and along strike, respectively.

| Figure | $\theta$ [deg] | $\alpha$ [ ] | C [ ] | Horizontal Distance between the trench and downdip of locked zone [km] | Transition zone width [km] |
|---|---|---|---|---|---|
| 2A Cascadia | 10 (*92*) | 0.2* | 0.05 | 39.6 | 59.7 |
| 2B Himalayas | Varying (*28*) | 0.2 | 0.05 | 86.5 | 19.9 |
| 2C Chile | Varying (*92*) | 0.2 | 0.05 | 80.3 | 20.0 |
| 3A | 7** | 0.2 | 0.05 | 30-205 | 50 |
| 3B | 7 | 0.2 | 0.05 | 65-90 | 50 |
| S2 | 10 | 0.2 | 0.05 | 100 | 50 |
| S9A | 7 | 0.2 | 0.05 | 100 | 25-75 |
| S9B | 7 | 0.2 | 0.025-0.4 | 100 | 50 |
| S9C | 5-17 | 0.2 | 0.05 | 100 | 50 |
| S9D | 7 | 0-0.4 | 0.05 | 100 | 50 |
| S10 | 7 | 0.2 | 0.05-0.4 | 30-205 | 50 |
| S11 | 7 | 0.2 | 0.05 | 100 | 50 |

Table S1 - Model parameters presented in the main text and Supplementary information.
* Based on the suggested value in the literature (*34*).
**Corresponds to the average dip angle of forearcs examined by Malatesta et al.(*13*).

## References


1. Lay, H. Kanamori, C. J. Ammon, K. D. Koper, A. R. Hutko, L. Ye, H. Yue, T. M. Rushing, Depth-varying rupture properties of subduction zone megathrust faults. *Journal of Geophysical Research: Solid Earth*. **117**, 1–21 (2012).

2. E. A. Wirth, V. J. Sahakian, L. M. Wallace, D. Melnick, The occurrence and hazards of great subduction zone earthquakes. *Nat Rev Earth Environ*. **3**, 125–140 (2022).

3. K. Wang, Y. Hu, J. He, Deformation cycles of subduction earthquakes in a viscoelastic Earth. *Nature*. **484**, 327–332 (2012).

4. R. Bürgmann, M. G. Kogan, G. M. Steblov, G. Hilley, V. E. Levin, E. Apel, Interseismic coupling and asperity distribution along the Kamchatka subduction zone. *Journal of Geophysical Research: Solid Earth*. **110** (2005), doi:10.1029/2005JB003648.

5. J. C. Savage, A dislocation model of strain accumulation and release at a subduction zone. *Journal of Geophysical Research* (1983), doi:10.1029/JB088iB06p04984.

6. B. W. Tichelaar, L. J. Ruff, Depth of seismic coupling along subduction zones. *Journal of Geophysical Research: Solid Earth*. **98**, 2017–2037 (1993).

7. E. M. Hill, J. C. Borrero, Z. Huang, Q. Qiu, P. Banerjee, D. H. Natawidjaja, P. Elosegui, H. M. Fritz, B. W. Suwargadi, I. R. Pranantyo, L. Li, K. A. Macpherson, V. Skanavis, C. E. Synolakis, K. Sieh, The 2010 Mw 7.8 Mentawai earthquake: Very shallow source of a rare tsunami earthquake determined from tsunami field survey and near-field GPS data. *Journal of Geophysical Research: Solid Earth*. **117** (2012), doi:10.1029/2012JB009159.

8. E. O. Lindsey, R. Mallick, J. A. Hubbard, K. E. Bradley, R. V. Almeida, J. D. P. Moore, R. Bürgmann, E. M. Hill, Slip rate deficit and earthquake potential on shallow megathrusts. *Nat. Geosci.* **14**, 321–326 (2021).

9. C. H. Scholz, Earthquakes and friction laws. *Nature*. **391**, 37–42 (1998).

10. B. Oryan, W. R. Buck, Larger tsunamis from megathrust earthquakes where slab dip is reduced. *Nature Geoscience* (2020), doi:10.1038/s41561-020-0553-x.

11. R. E. Wells, R. J. Blakely, Y. Sugiyama, D. W. Scholl, P. A. Dinterman, Basin-centered asperities in great subduction zone earthquakes: A link between slip, subsidence, and subduction erosion?: COSEISMIC SLIP IN GREAT EARTHQUAKES. *J. Geophys. Res.* **108** (2003), doi:10.1029/2002JB002072.

12. T.-R. A. Song, M. Simons, Large Trench-Parallel Gravity Variations Predict Seismogenic Behavior in Subduction Zones. *Science*. **301**, 630–633 (2003).

13. L. C. Malatesta, L. Bruhat, N. J. Finnegan, J.-A. L. Olive, *Journal of Geophysical Research: Solid Earth*, in press, doi:10.1029/2020JB019589.

14. J. Lavé, J. P. Avouac, Fluvial incision and tectonic uplift across the Himalayas of central Nepal. *Journal of Geophysical Research: Solid Earth*. **106**, 26561–26591 (2001).

15. B. J. Meade, The signature of an unbalanced earthquake cycle in Himalayan topography? *Geology*. **38**, 987–990 (2010).

16. F. J. Clubb, S. M. Mudd, T. F. Schildgen, P. A. van der Beek, R. Devrani, H. D. Sinclair, Himalayan valley-floor widths controlled by tectonically driven exhumation. *Nat. Geosci.* **16**, 739–746 (2023).

17. M. Jackson, R. Bilham, Constraints on Himalayan deformation inferred from vertical velocity fields in Nepal and Tibet. *Journal of Geophysical Research: Solid Earth*. **99**, 13897–13912 (1994).

18. K. M. Sreejith, P. S. Sunil, R. Agrawal, A. P. Saji, A. S. Rajawat, D. S. Ramesh, Audit of stored strain energy and extent of future earthquake rupture in central Himalaya. *Sci Rep*. **8**, 16697 (2018).

19. B. Rousset, C. Lasserre, N. Cubas, S. Graham, M. Radiguet, C. DeMets, A. Socquet, M. Campillo, V. Kostoglodov, E. Cabral-Cano, N. Cotte, A. Walpersdorf, Lateral Variations of Interplate Coupling along the Mexican Subduction Interface: Relationships with Long-Term Morphology and Fault Zone Mechanical Properties. *Pure Appl. Geophys.* **173**, 3467–3486 (2016).

20. M. Saillard, L. Audin, B. Rousset, J.-P. Avouac, M. Chlieh, S. R. Hall, L. Husson, D. L. Farber, From the seismic cycle to long-term deformation: linking seismic coupling and Quaternary coastal geomorphology along the Andean megathrust. *Tectonics*. **36**, 241–256 (2017).

21. D. Melnick, Rise of the central Andean coast by earthquakes straddling the Moho. *Nature Geoscience*. **9**, 401–407 (2016).

22. R. Jolivet, M. Simons, Z. Duputel, J. Olive, H. S. Bhat, Q. Bletery, Interseismic loading of subduction megathrust drives long term uplift in northern Chile, 1–21 (2020).

23. A. Madella, T. A. Ehlers, Contribution of background seismicity to forearc uplift. *Nat. Geosci.*, 1–6 (2021).

24. C. W. Baden, D. L. Shuster, F. Aron, J. C. Fosdick, R. Bürgmann, G. E. Hilley, Bridging earthquakes and mountain building in the Santa Cruz Mountains, CA. *Science Advances*. **8**, eabi6031 (2022).

25. G. C. P. King, R. S. Stein, J. B. Rundle, The Growth of Geological Structures by Repeated Earthquakes 1. Conceptual Framework. *Journal of Geophysical Research: Solid Earth*. **93**, 13307–13318 (1988).

26. T. Nishimura, Pre-, Co-, and Post-Seismic Deformation of the 2011 Tohoku-Oki Earthquake and its Implication to a Paradox in Short-Term and Long-Term Deformation. *J. Disaster Res.* **9**, 294–302 (2014).

27. V. Mouslopoulou, O. Oncken, S. Hainzl, A. Nicol, Uplift rate transients at subduction margins due to earthquake clustering. *Tectonics*. **35**, 2370–2384 (2016).

28. J. R. Elliott, R. Jolivet, P. J. González, J.-P. Avouac, J. Hollingsworth, M. P. Searle, V. L. Stevens, Himalayan megathrust geometry and relation to topography revealed by the Gorkha earthquake. *Nature Geosci*. **9**, 174–180 (2016).

29. B. Oryan, P. M. Betka, M. S. Steckler, S. L. Nooner, E. O. Lindsey, D. Mondal, A. M. Mathews, S. H. Akhter, S. Singha, O. Than, *JGR Solid Earth*, in press, doi:10.1029/2022JB025550.

30. M. S. Paterson, T. Wong, *Experimental Rock Deformation — The Brittle Field* (Springer-Verlag, Berlin/Heidelberg, 2005; http://link.springer.com/10.1007/b137431).

31. R. Cattin, J. P. Avouac, Modeling mountain building and the seismic cycle in the Himalaya of Nepal. *Journal of Geophysical Research: Solid Earth*. **105**, 13389–13407 (2000).

32. D. Davis, J. Suppe, F. A. Dahlen, Mechanics of fold-and-thrust belts and accretionary wedges. *J. Geophys. Res.* **88**, 1153 (1983).

33. I. Stone, J. E. Vidale, S. Han, E. Roland, Catalog of Offshore Seismicity in Cascadia: Insights Into the Regional Distribution of Microseismicity and its Relation to Subduction Processes. *Journal of Geophysical Research: Solid Earth* (2018), doi:10.1002/2017JB014966.

34. J. Dieterich, A constitutive law for rate of earthquake production and its application to earthquake clustering. *Journal of Geophysical Research: Solid Earth*. **99**, 2601–2618 (1994).

35. J. Dieterich, V. Cayol, P. Okubo, The use of earthquake rate changes as a stress meter at Kilauea volcano. *Nature*. **408**, 457–460 (2000).

36. D. L. Wells, K. J. Coppersmith, New empirical relationships among magnitude, rupture length, rupture width, rupture area, and surface displacement. *Bulletin of the Seismological Society of America*. **84**, 974–1002 (1994).

37. Y. Okada, Surface deformation due to shear and tensile faults in a half-space. *International Journal of Rock Mechanics and Mining Sciences & Geomechanics Abstracts*. **23**, 128 (1986).

38. Y. Okada, Internal deformation due to shear and tensile faults in a half-space. *Bulletin - Seismological Society of America* (1992).

39. A. R. Nelson, H. M. Kelsey, R. C. Witter, Great earthquakes of variable magnitude at the Cascadia subduction zone. *Quat. res.* **65**, 354–365 (2006).

40. V. V. Kostrov, Seismic moment and energy of earthquakes, and seismic flow of rock. *International Journal of Rock Mechanics and Mining Sciences & Geomechanics Abstracts*. **13**, A4 (1976).

41. C. D. Peterson, K. M. Cruikshank, Quaternary Tectonic Deformation, Holocene Paleoseismicity, and Modern Strain in the Unusually–Wide Coupled Zone of the Central Cascadia Margin, Washington and Oregon, USA, and British Columbia, Canada. *JGG*. **6**, p1 (2014).

42. T. Ader, J.-P. Avouac, J. Liu-Zeng, H. Lyon-Caen, L. Bollinger, J. Galetzka, J. Genrich, M. Thomas, K. Chanard, S. N. Sapkota, S. Rajaure, P. Shrestha, L. Ding, M. Flouzat, Convergence rate across the Nepal Himalaya and interseismic coupling on the Main Himalayan Thrust: Implications for seismic hazard. *Journal of Geophysical Research: Solid Earth*. **117** (2012), doi:10.1029/2011JB009071.

43. S. Rajaure, S. N. Sapkota, L. B. Adhikari, B. Koirala, M. Bhattarai, D. R. Tiwari, U. G. Gautam, P. Shrestha, S. Maske, J. P. Avouac, L. Bollinger, M. R. Pandey, Double difference relocation of local earthquakes in the Nepal Himalaya. *Journal of Nepal Geological Society*. **46**, 133–142 (2013).

44. C. Sippl, B. Schurr, G. Asch, J. Kummerow, Seismicity Structure of the Northern Chile Forearc From >100,000 Double-Difference Relocated Hypocenters. *Journal of Geophysical Research: Solid Earth*. **123**, 4063–4087 (2018).

45. V. Godard, D. L. Bourles, F. Spinabella, D. W. Burbank, B. Bookhagen, G. B. Fisher, A. Moulin, L. Leanni, Dominance of tectonics over climate in Himalayan denudation. *Geology*. **42**, 243–246 (2014).

46. L. Dal Zilio, G. Hetényi, J. Hubbard, L. Bollinger, Building the Himalaya from tectonic to earthquake scales. *Nat Rev Earth Environ*. **2**, 251–268 (2021).

47. V. Godard, D. W. Burbank, D. L. Bourlès, B. Bookhagen, R. Braucher, G. B. Fisher, Impact of glacial erosion on $^{10}$Be concentrations in fluvial sediments of the Marsyandi catchment, central Nepal. *J. Geophys. Res.* **117**, 2011JF002230 (2012).

48. J.-P. Avouac, "MOUNTAIN BUILDING, EROSION, AND THE SEISMIC CYCLE IN THE NEPAL HIMALAYA" in *Advances in Geophysics* (Elsevier, 2003; https://linkinghub.elsevier.com/retrieve/pii/S0065268703460019), vol. 46, pp. 1–80.

49. S. Ruiz, R. Madariaga, Historical and recent large megathrust earthquakes in Chile. *Tectonophysics*. **733**, 37–56 (2018).

50. A. R. Niemeijer, C. J. Spiers, Compaction creep of quartz-muscovite mixtures at 500°C: Preliminary results on the influence of muscovite on pressure solution. *Geological Society, London, Special Publications*. **200**, 61–71 (2002).

51. N. Brantut, P. Baud, M. J. Heap, P. G. Meredith, Micromechanics of brittle creep in rocks. *Journal of Geophysical Research: Solid Earth* (2012), doi:10.1029/2012JB009299.

52. S. Ma, A self-consistent mechanism for slow dynamic deformation and tsunami generation for earthquakes in the shallow subduction zone. *Geophysical Research Letters*. **39** (2012), doi:10.1029/2012GL051854.

53. A. Baker, R. W. Allmendinger, L. A. Owen, J. A. Rech, Permanent deformation caused by subduction earthquakes in northern Chile. *Nature Geosci*. **6**, 492–496 (2013).

54. Y. Hu, K. Wang, Coseismic strengthening of the shallow portion of the subduction fault and its effects on wedge taper. *Journal of Geophysical Research: Solid Earth*. **113** (2008), doi:https://doi.org/10.1029/2008JB005724.

55. M. Y. Thomas, H. S. Bhat, Dynamic evolution of off-fault medium during an earthquake: a micromechanics based model. *Geophysical Journal International*. **214**, 1267–1280 (2018).

56. N. Cubas, P. Agard, R. Tissandier, Earthquake ruptures and topography of the Chilean margin controlled by plate interface deformation. *Solid Earth*. **13**, 779–792 (2022).

57. L. Dal Zilio, J. Ruh, J.-P. Avouac, *Tectonics*, in press, doi:10.1029/2020TC006210.

58. A. Noda, Forearc basins: Types, geometries, and relationships to subduction zone dynamics. *GSA Bulletin*. **128**, 879–895 (2016).

59. E. Tam, Y. Yokoyama, A review of MIS 5e sea-level proxies around Japan. *Earth System Science Data*. **13**, 1477–1497 (2021).

60. Y. Niwa, T. Sugai, Y. Matsushima, S. Toda, Millennial-scale crustal movements inferred from Holocene sedimentary succession of the Omoto plain, northern Sanriku coast, Northeast Japan: Relevance for modeling megathrust earthquake cycles. *Quaternary International*. **519**, 10–24 (2019).

61. Y. Hu, R. Bürgmann, N. Uchida, P. Banerjee, J. T. Freymueller, Stress-driven relaxation of heterogeneous upper mantle and time-dependent afterslip following the 2011 Tohoku earthquake. *Journal of Geophysical Research: Solid Earth*. **121**, 385–411 (2016).

62. R. J. Burgette, R. J. Weldon, D. A. Schmidt, Interseismic uplift rates for western Oregon and along-strike variation in locking on the Cascadia subduction zone: CASCADIA INTERSEISMIC UPLIFT AND LOCKING. *J. Geophys. Res.* **114** (2009), doi:10.1029/2008JB005679.

63. A. Helmstetter, B. E. Shaw, Relation between stress heterogeneity and aftershock rate in the rate-and-state model. *Journal of Geophysical Research: Solid Earth*. **111** (2006), doi:10.1029/2005JB004077.

64. K. A. Kroll, K. B. Richards-Dinger, J. H. Dieterich, E. S. Cochran, Delayed Seismicity Rate Changes Controlled by Static Stress Transfer. *Journal of Geophysical Research: Solid Earth*. **122**, 7951–7965 (2017).

65. S. Toda, R. S. Stein, T. Sagiya, Evidence from the AD 2000 Izu islands earthquake swarm that stressing rate governs seismicity. *Nature*. **419**, 58–61 (2002).

66. S. Toda, R. S. Stein, Central shutdown and surrounding activation of aftershocks from megathrust earthquake stress transfer. *Nat. Geosci.* **15**, 494–500 (2022).

67. E. S. Cochran, J. E. Vidale, S. Tanaka, Earth Tides Can Trigger Shallow Thrust Fault Earthquakes. *Science*. **306**, 1164–1166 (2004).

68. C. H. Scholz, Y. J. Tan, F. Albino, The mechanism of tidal triggering of earthquakes at mid-ocean ridges. *Nat Commun*. **10**, 2526 (2019).

69. T. Parsons, S. Toda, R. S. Stein, A. Barka, J. H. Dieterich, Heightened Odds of Large Earthquakes Near Istanbul: An Interaction-Based Probability Calculation. *Science*. **288**, 661–665 (2000).

70. R. S. Stein, A. A. Barka, J. H. Dieterich, Progressive failure on the North Anatolian fault since 1939 by earthquake stress triggering. *Geophysical Journal International*. **128**, 594–604 (1997).

71. F. Cappa, M. M. Scuderi, C. Collettini, Y. Guglielmi, J.-P. Avouac, Stabilization of fault slip by fluid injection in the laboratory and in situ. *Science Advances*. **5**, eaau4065 (2019).

72. B. H. Hager, J. Dieterich, C. Frohlich, R. Juanes, S. Mantica, J. H. Shaw, F. Bottazzi, F. Caresani, D. Castineira, A. Cominelli, M. Meda, L. Osculati, S. Petroselli, A. Plesch, A process-based approach to understanding and managing triggered seismicity. *Nature*. **595**, 684–689 (2021).

73. E. R. Heimisson, J. D. Smith, J.-P. Avouac, S. J. Bourne, Coulomb threshold rate-and-state model for fault reactivation: application to induced seismicity at Groningen. *Geophysical Journal International*. **228**, 2061–2072 (2022).

74. E. R. Heimisson, P. Segall, Constitutive Law for Earthquake Production Based on Rate-and-State Friction: Dieterich 1994 Revisited. *Journal of Geophysical Research: Solid Earth*. **123**, 4141–4156 (2018).

75. P. Segall, S. Lu, Injection-induced seismicity: Poroelastic and earthquake nucleation effects. *Journal of Geophysical Research: Solid Earth*. **120**, 5082–5103 (2015).

76. R. Almeida, E. O. Lindsey, K. Bradley, J. Hubbard, R. Mallick, E. M. Hill, Can the Updip Limit of Frictional Locking on Megathrusts Be Detected Geodetically? Quantifying the Effect of Stress Shadows on Near-Trench Coupling. *Geophysical Research Letters*. **45**, 4754–4763 (2018).

77. B. Gutenberg, C. Richter, *Seismicity of the Earth and Associated Phenomena* (Princeton University Press, ed. 2nd, 1954).

78. V. L. Stevens, J.-P. Avouac, On the relationship between strain rate and seismicity in the India–Asia collision zone: implications for probabilistic seismic hazard. *Geophysical Journal International*. **226**, 220–245 (2021).

79. D. Schorlemmer, S. Wiemer, M. Wyss, Variations in earthquake-size distribution across different stress regimes. *Nature*. **437**, 539–42 (2005).

80. S. Carretier, V. Tolorza, V. Regard, G. Aguilar, M. A. Bermúdez, J. Martinod, J.-L. Guyot, G. Hérail, R. Riquelme, Review of erosion dynamics along the major N-S climatic gradient in Chile and perspectives. *Geomorphology*. **300**, 45–68 (2018).

81. P. Molnar, Climate change, flooding in arid environments, and erosion rates. *Geology*. **29**, 1071–1074 (2001).

82. A. T. Codilean, H. Munack, W. M. Saktura, T. J. Cohen, Z. Jacobs, S. Ulm, P. P. Hesse, J. Heyman, K. J. Peters, A. N. Williams, R. B. K. Saktura, X. Rui, K. Chishiro-Dennelly, A. Panta, OCTOPUS database (v.2). *Earth System Science Data*. **14**, 3695–3713 (2022).

83. C. Placzek, D. E. Granger, A. Matmon, J. Quade, U. Ryb, Geomorphic process rates in the central Atacama Desert, Chile: Insights from cosmogenic nuclides and implications for the onset of hyperaridity. *American Journal of Science*. **314**, 1462–1512 (2014).

84. D. Lague, The stream power river incision model: evidence, theory and beyond. *Earth Surface Processes and Landforms*. **39**, 38–61 (2014).

85. P. Vásquez, F. Sepulveda, A. Quezada, S. Aguilef, C. Franco, N. Blanco, Cartas Guanillos de Norte y Salar de Llamara 1:100.000, regiones de Tarapacá y Antofagasta, Chile. (2018), doi:10.13140/RG.2.2.36060.41600.

86. B. Gailleton, S. M. Mudd, Lsdtopotools/lsdtopytools: lsdtopytools (2021).

87. J. Takaku, T. Tadono, K. Tsutsui, Generation of High Resolution Global DSM from ALOS PRISM. *The International Archives of the Photogrammetry, Remote Sensing and Spatial Information Sciences*. **XL–4**, 243–248 (2014).

88. Y. Y. Kagan, Seismic moment distribution revisited: I. Statistical results. *Geophysical Journal International*. **148**, 520–541 (2002).

89. R. F. Mereu, A study of the relations between ML, Me, Mw, apparent stress, and fault aspect ratio. *Physics of the Earth and Planetary Interiors*. **298**, 106278 (2020).

90. V. L. Stevens, S. N. Shrestha, D. K. Maharjan, Probabilistic Seismic Hazard Assessment of Nepal. *Bulletin of the Seismological Society of America*. **108**, 3488–3510 (2018).

91. V. L. Stevens, J. -P. Avouac, Determination of Mmax from Background Seismicity and Moment Conservation. *Bulletin of the Seismological Society of America*. **107**, 2578–2596 (2017).

92. G. P. Hayes, G. L. Moore, D. E. Portner, M. Hearne, H. Flamme, M. Furtney, G. M. Smoczyk, Slab2, a comprehensive subduction zone geometry model. *Science*. **362**, 58–61 (2018).